

STUDY OF STRUCTURE-PROPERTY-PERFORMANCE RELATIONSHIPS FOR
ORGANIC THIN-FILM TRANSISTORS AND POLYMERIC SOLAR CELLS

by

SHENG BI

DAWEN LI, COMMITTEE CHAIR
TIM A. HASKEW
PAUL A. RUPAR
FEI HU
QING PENG

A DISSERTATION

Submitted in partial fulfillment of the requirements
for the degree of Doctor of Philosophy
in the Department of Electrical and Computer Engineering
in the Graduate School of
The University of Alabama

TUSCALOOSA, ALABAMA

2016

Copyright Sheng Bi 2016
ALL RIGHTS RESERVED

ABSTRACT

Organic electronics has great potential for fabricating low cost, flexible and large-area devices. Despite the rapid development, several main challenges of the field need to be addressed in both organic conjugated polymer and small molecules based devices, including organic thin-film transistors (OTFTs) and polymer solar cells (PSCs).

This dissertation first explores two approaches to align small molecule crystals and improve surface coverage. The controlled evaporative self-assembly (CESA) method is combined with binary solvent system using small molecule SMDPPEH to control the crystal growth. By optimizing the two solvent ratios, well-aligned SMDPPEH crystals with significantly improved areal coverage were achieved. Also, polymer additives can be added into small molecule to control crystal alignment. As a result, mobilities are at least 10 times higher than that from spin-coated film. The SMDPPEH based OTFTs exhibit a mobility of $1.6 \times 10^{-2} \text{ cm}^2/\text{Vs}$, which is the highest mobility from SMDPPEH ever reported.

The donor-acceptor vertical composition profile on the performance of the P3HT/PCBM based organic bulk heterojunction solar cells was studied. In this simulation study, variety of donor-acceptor vertical configurations was investigated for both regular and inverted PSC structures. The physical mechanisms behind the diversification of open circuit voltage, short circuit current, and fill factor, and thus power conversion efficiency from various vertical

configurations are explained. The effect of vertical composition profile from the study could serve as guidance for experimental optimization of organic bulk heterojunction solar cells.

Also, morphology variation of ZnO electron transport layer from atomic layer deposition and sol-gel methods on the performance of organic inverted solar cells were investigated. AFM and SEM were utilized to characterize the morphology of ZnO thin films and nanorods so as to explain the efficiency difference.

The final part of the work demonstrates one-step multi-layer pattern transfer to make organic solar cells on rigid and flexible substrates. A multi-layer inking and stamping, a cost-efficient, purely additive pattern transfer technique, was developed to fabricate PSCs. GLYMO is added into PEDOT:PSS hole transport layer and its effect on PSC performance and pattern transfer yield was investigated to reach overall PSC efficiency and high yield pattern transfer.

DEDICATION

This dissertation is dedicated to everyone who has helped me and guided me through the trials and tribulations of creating this manuscript.

LIST OF ABBREVIATIONS AND SYMBOLS

C_i	Capacitance per unit area of the dielectric layer
ε	Permittivity
E_F	Fermi level
k	Boltzmann's constant
ρ	Density of charge carriers (hole or electron)
q	Charge of charge carriers (hole or electron)
μ	Field-effect mobility
n	Electron density
p	Hole density
V_{OC}	Open circuit voltage
I_{SC}	Short circuit current
FF	Fill factor
PCE	Power conversion efficiency

ACKNOWLEDGEMENTS

I am pleased to take this chance to thank the many colleagues, friends, and professors who have helped me with my Ph. D. study and research at The University of Alabama. Otherwise, it would have been impossible for me to write this dissertation.

Firstly, above all my deepest gratitude goes to Dr. Dawen Li for giving me the opportunity to carry out this project in his group and for his supervision and guidance along the project. I genuinely thank him for his continuous positive and encouraging attitude and I thank him for always being a great leader to look up to. I finally thank him for all the projects, tasks and challenges that have been given to me and that helped me increase significantly my knowledge in the field.

Next, I would like to express my great gratitude for my committee members, Dr. Fei Hu, Dr. Qing Peng, Dr. Paul A. Rugar and Dr. Tim A. Haskew, for their valuable scientific discussions and advices, and inspiring questions of both my academic study and dissertation writing.

Also, I would like to thank my colleagues for their help and suggestions for my research. I would like to thank Dr. Jihua Chen at Oak Ridge National Laboratory for his help on the transmission electron microscopy, and Mr. Zhongliang Ouyang, Mr. Shoieb Shaik, Ms. Kyeiwaa Asare-Yeboah and Mr. Chengming Jiang for their help and great discussion of my research.

Finally, I would like to express my thankfulness to my family who has always been supportive of me for every decision I make. Their great love, care and understanding is the most motivation with which I complete my Ph. D. study and research.

CONTENTS

ABSTRACT.....	ii
DEDICATION.....	iv
LIST OF ABBREVIATION AND SYMBOLS	v
ACKNOWLEDGEMENTS.....	vi
LIST OF TABLES.....	xi
LIST OF FIGURES	xii
CHAPTER 1.INTRODUCTION	1
1.1 Overview of Organic Electronics and Semiconductors	1
1.2 Organic Thin-Film Transistors (OTFTs)	3
1.2.1. Introduction to OTFTs	3
1.2.2. Architectures of OTFTs and Operational Mechanism	4
1.3 Organic PolymerSolar Cells (PSCs)	6
1.3.1 Introduction to Organic Polymer Solar Cells.....	6
1.3.2 Operational Mechanism of Bulk Heterojunction Solar Cells and Architectures	9
CHAPTER 2. SOLUTION-GROWN SMALL-MOLECULE ORGANIC SEMICONDUCTOR WITH ENHANCED CRYSTAL ALIGNMENT AND AREAL COVERAGE FOR ORGANIC THIN FILM TRANSISTORS	12
2.1 Introduction	12
2.2 Experiment	14
2.3 Result and Discussion	17

2.4 Crystal Alignment by Interaction Between Small Molecule and P3HT Conjugated Polymer	26
2.5 Conclusion.....	31
CHAPTER 3. INFLUENCE OF VERTICAL COMPOSITION PROFILE ON EFFICIENCY OF ORGANIC POLYMERIC SOLAR CELLS	32
3.1 Introduction	32
3.2 Model Establishment and Simulation Parameters.....	34
3.3 Result and Discussion	39
3.4 Vertical Configuration in Inverted Solar Cell Structure	43
3.5 Summary and Conclusion	50
CHAPTER 4. STUDY OF DIFFERENT MORPHOLOGY OF ZNO FILMS PREPARED BY MULTI-METHODS AND THEIR EFFECT ON SOLAR CELL.....	52
4.1 Introduction	52
4.2 Experiment	54
4.3 Result and Discussion	55
4.4 Conclusion.....	58
CHAPTER 5. POLYMER SOLAR CELL FABRICATION BY MULTI-LAYER INKING AND STAMPING	60
5.1 Introduction	60
5.2 Experiment	62
5.3 Result and Discussion	65
5.4 Conclusion.....	71
CHAPTER 6. CONCLUSIONS AND FUTURE WORK.....	73
6.1 Conclusion.....	73
6.2 Future Work	76

REFERENCES	80
APPENDIX.....	90

LIST OF TABLES

3.1 Electronic parameters of P3HT/PCBM blend at different PCBM percentages···	37
4.1 Solar cell performance with different kinds of ZnO deposition methods.....	56
5.1 Voc (V), Jsc (mA/cm ²), FF(%), and efficiency values of spin-coated solar cells with various amounts of GLYMO added into 1ml of PEDOT:PSS solution.....	70

LIST OF FIGURES

1.1 Molecular orbital diagram with HOMO and LUMO energy levels at a) ground state. b) excited state.....	3
1.2 Architecture of organic thin-film transistors/field effect transistor	5
1.3 (a) bottom-gate, top-contact OTFT configuration, and (b) bottom-gate, bottom-contact OTFT configuration.....	6
1.4 Sketch of (a) single layer, (b) bilayer, (c) bulk heterojunction polymer solar cell structures.....	9
1.5 Schematics of (a) exciton generation/dissociation and charge transport , and (b) energy band diagram in organic polymer solar cells	10
1.6 Configurations of polymer solar cells: (a) regular structure, and (b) inverted structure....	11
2.1 (a) Molecular structure of SMDPPEH. Optical image of SMDPPEH crystals drop casted in (b) single chloroform solvent and (c) chloroform/ethanol (5:1) double solvents.....	14
2.2 .(a) Schematic of the CESA method for crystal alignment. (b) The zoom in optical image of SMDPPEH films with highly orientated crystals and great film coverage. The scale bar represents 50 μm . (c) digital image of crystal growth over entire substrate with chloroform/ethanol ratio of 5:1.....	16
2.3 Optical micrographs of SMDPPEH crystals drop casted from chloroform/ethanol double solvents at different ratios: (a) 15:1, (b) 10:1, (c) 5:1, (d) 1:1 and (e) 1:5, respectively. All images share the same scale bar of 100 μm as shown in (a). (f) Effect of nucleation seed density on crystallization.....	19
2.4 Quantitative analysis of the (a) average crystal misorientation, (b) film coverage, and (c) average crystal width of the SMDPPEH crystals at different ratios of the chloroform/ethanol double solvents.....	22
2.5 (a) Schematic of bottom-gate, bottom-contact OTFTs with SMDPPEH crystal ribbons as active layer. (b) Transfer characteristics for field-effect mobility extraction. The volume ratio of chloroform to ethanol solvent is 5:1. (c) Mobility variation of SMDPPEH OTFTs based on different types of films.....	25

2.6 Optical images of SMDPPEH and P3HT blends at different ratios and concentrations. (a)-(c) Ratio of SMDPPEH to P3HT varies from 1:1 to 10:1 at the same concentration of 2mg/ml. (d)-(f) Different concentration of SMDPPEH and P3HT solution at the same ratio of 5:1. All optical images share the same scale bar.....	28
2.7 Schematic of bottom-gate, top-contact OTFTs with SMDPPEH and P3HT blend crystal ribbons as active layer. (b) Output and (c) transfer characteristics. The volume ratio of SMDPPEH to P3HT is 5:1 with the concentration of 2mg/ml	30
3.1 Schematic of the vertical composition profile of (a) sandwich I, (b) sandwich II, (c) charge transport favorable, (d) unfavorable, (e) uniform configuration of active layer in regular PSC structure, and (f) direction of charge carriers transport in the active layer. ...	36
3.2 (a) J-V characteristics from SETFOS simulation, and (b) PSC efficiencies of sandwich I, sandwich II, charge transport favorable, unfavorable and uniform vertical configurations	39
3.3 Solar cell output characteristics of (a) open circuit voltage, (b) absorbance spectrum, (c) short circuit current, (d) external quantum efficiency, (e) fill factor, and (f) equivalent circuit	42
3.4 Energy band diagram of (a) sandwich I, (b) sandwich II, (c) favorable and (d) unfavorable configuration.....	43
3.5 Schematic of (a) direction of electrons and holes transport in the active layer, and various vertical composition profiles (b) sandwich I, (c) sandwich II, (d) charge transport favorable, (e) unfavorable, and (f) uniform configuration of active layer in inverted PSC structure.....	45
3.6 (a) J-V characteristics from SETFOS simulation, and (b) PSC efficiencies of sandwich I, sandwich II, charge transport favorable, unfavorable and uniform vertical configurations	46
3.7 Solar cell output characteristics of (a) absorbance spectrum, (b) external quantum efficiency, (c) short circuit current, (d) open circuit voltage, (e) fill factor, and (f) equivalent circuit.....	48
3.8 Energy band diagram of (a) favorable, (b) unfavorable, (c) sandwich I and (d) sandwich II configuration	50
4.1 Schematic of (a) ZnO film, and (b) ZnO nanorods in P3HT-PCBM based inverted solar cells.....	53
4.2 Comparison of I-V curves for inverted solar cells with ZnO from ALD, sol-gel method, ALD seeded nanorods and sol-gel seeded nanorods.....	56

4.3 SEM image of ZnO nanorods from (a) sol-gel seeded method and (b) ALD seeded method. Inset monograph is the side-view of nanorods. AFM image of (c) sol-gel film and (d) ALD deposited film.....	58
5.1 Chemical structures of (a) P3HT, (b) PCBM and (c) GLYMO.....	64
5.2 Schematic of the multilayer inking and stamping technique. Multilayer inking onto PDMS stamp following by stamping on plasma treated ITO glass. Multilayer organic solar cells are fabricated after peeling off the PDMS stamp from ITO glass.	65
5.3 (a) SEM monograph of a high yield pattern transfer onto ITO glass substrate. (b) AFM image of the recession between two separated patterns after the pattern transfer process. (c) SEM cross-sectional image of the transferred multi-layers, Au/Al, P3HT/PCBM, PEDOT:PSS, from top to bottom on ITO glass. (d) Optical photograph of multi-layer PSCs successfully transferred onto a PET flexible substrate.....	67
5.4 (a) I-V characterizations of spin-coated P3HT/PCBM solar cells with 0.0 μ l, 2.5 μ l, 5.0 μ l, 10.0 μ l and 20.0 μ l of GLYMO added into 1ml of PEDOT:PSS solution. (b) Comparison of PSC efficiency vs. the amount of GLYMO added into 1ml of PEDOT:PSS solution..	70
5.5 I-V characterization of the PSC devices (Au/Al/P3HT/PCBM/PEDOT:PSS/ITO) fabricated by the multi-layer inking and stamping.....	71
6.1 Schematic of perovskite solar cells with (a) regular and (b) inverted structures.....	78

CHAPTER 1

INTRODUCTION

1.1 Overview of Organic Electronics and Semiconductors

Organic electronics has received worldwide attention due to great potential for fabricating low cost, flexible and large-area devices.¹⁻³ It is a field about synthesis, design and application of organic materials. Organic electronics consists of a wide range of devices including organic field effect transistors (OFETs)^{4, 5}, polymer solar cells (PSCs)^{6, 7} and organic light emitting diodes (OLEDs)^{8, 9}.

Based on molecular weight, there are two classes of organic semiconductors: small molecules and polymers. Small molecules have a low molecular weight and single unit, while polymers tend to consist of long chains of repeating monomeric units. Small molecules are easily purified by thermal sublimation to achieve impurity concentration of less than 10^{-4} . Also organic small molecule semiconductors have a better crystallinity, which helps to improve charge transport.^{10, 11} The main drawback of small molecules is that they are usually hard to dissolve in organic solvents, which makes them difficult to deposit using solution processing but from gas phase via sublimation or evaporation.^{12, 13} For polymers, they can be purified by chromatography but difficult to attain impurity concentration less than 1%. Meanwhile, they are mostly semicrystalline with amorphous regions after deposition, leading to poor charge transport mobility.¹⁴ The positive side is that their solubility in organic solvents is much better than small

molecules, which makes them suitable for solution processing.¹⁵ For organic polymers, the difference in molecular weight has an enormous effect on crystallization, crystal orientation and device performance, usually the higher the molecular weight, the better the crystallization and charge transport.^{16, 17}

All organic semiconductors have in common a conjugated π -electron system. Conjugated π -electron system is organic macromolecules whose backbones consist of alternating double- and single-bonds. Conjugated π -electron system in organic semiconductors is formed by the p_z -orbital of sp^2 -hybridized carbon atoms or lone electron pairs in the molecules.^{9, 18} The lowest electronic excitations of conjugated molecules are the π - π^* -transitions with an energy gap typically between 1.5 and 3 eV. The energy gap can be controlled by the degree of conjugation in a molecule and addition of side-groups. Thus, chemistry offers a wide range of possibilities to fine tune the energy gap thereby optoelectronic properties of organic semiconducting materials. Unlike inorganic semiconductors in which atoms are bonded by strong covalent bonds, organic molecules are bonded by weak Van der Waals force. As a result, organic semiconductors are usually amorphous or polycrystalline, soft and low melting points. Instead of having conduction band and valence band as in traditional inorganic semiconductors, organic semiconductors have energy structure of highest occupied molecular orbital (HOMO) and lowest unoccupied molecular orbital (LUMO) energy levels, which is essentially the gap between π - π^* molecular orbital.

Figure 1.1 shows the molecular orbital diagram of the simplest conjugated polymer Polyacetylene. When a photon with energy greater than HOMO-LUMO gap interacts with a polyacetylene molecule, the electrons can be excited from HOMO to LUMO energy level,

accordingly the molecule is transferred from ground state to an excited state, which is known as an excitation.

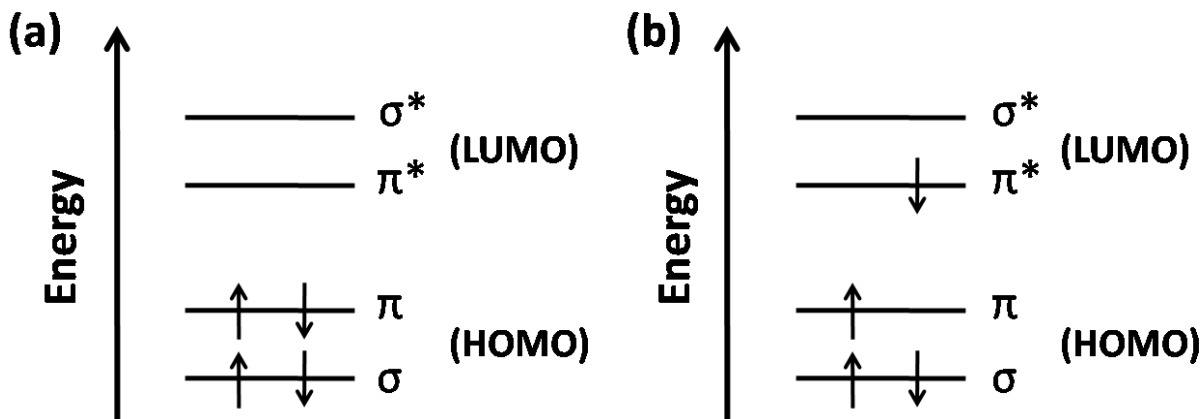


Figure 1.1 Molecular orbital diagram with HOMO and LUMO energy levels at a) ground state. b) excited state.

Other properties of organic semiconductors include hopping of charge carriers and low dielectric constant. Charges transport through hopping between molecules causes much lower mobility compared with inorganic semiconductors with energy band structure. Because of the weaker bonding between molecules, organic semiconductors show low dielectric constants around $\epsilon = 3 \sim 5$ compared to crystalline semiconductor with $\epsilon = 10 \sim 15$.¹⁹ The lower ϵ results in a lower shielding of charges and thus a stronger Coulomb interaction.

1.2 Organic Thin-Film Transistors (OTFTs)

1.2.1 Introduction to OTFTs

Organic thin-film transistor (OTFT), also called organic field-effect transistor (OFET), is a unipolar device with either electrons or holes as charge carrier for conducting current. OTFTs

can be easily fabricated at low temperature, suitable for flexible displays, and charge transport in organic semiconductors is comparable with that in amorphous silicon, which is dominant semiconductor in displays. Currently the highest field-effect mobility of $43\text{cm}^2/\text{Vs}$ has been demonstrated.²⁰ Despite the advantage of solution processibility at low temperature in making organic thin film transistors, the films obtained by both simple drop casting method and spin coating method typically exhibit random orientation of organic semiconductor crystals, small coverage of the substrate and aggregation.²¹ The uneven distribution of semiconductor crystals and their orientations causes severe OTFT performance variations. If such films are used as active layer of OTFTs to drive OLEDs in organic flexible displays, the brightness at different pixels will vary significantly. In addition, compared to inorganic semiconductors, organic devices are still much sensitive to air, water and UV light.²²

In this study, crystal alignment in solution processing and areal coverage on substrate are major topics addressed.

1.2.2 Architectures of OTFTs and Operational Mechanism

As illustrated in Figure 1.2, like any field-effect transistors, OTFTs have three electrodes: source, drain and gate. Charge carriers are injected from source contact to organic semiconductor. Gate electrode introduces vertical electric field to accumulate the charge carriers at the semiconductor/dielectric interface, forming conducting channel. Drain voltage creates lateral electric field in the channel for charge carriers to drift from source to drain. The applied voltage between the gate and source electrodes controls the concentration of accumulated charge

carriers thereby the conductivity in the channel. The voltage applied between drain and source electrode determines the electric field in the channel, thereby manipulating the drift current.

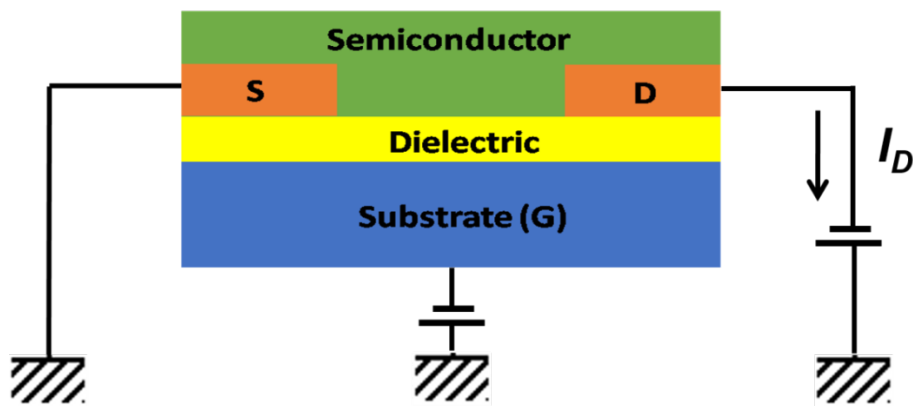


Figure 1.2 Architecture of organic thin-film transistors/field effect transistor.

There could be two kinds of vertical configurations depending on the position of gate electrode, top gate and bottom gate device. In this study, bottom gate structure is utilized. In bottom gate configuration, there are two ways of arranging source and drain electrodes, top-contact and bottom-contact, as shown in Figure 1.3. Bottom-gate, top-contact OTFTs normally demonstrate better device performances than bottom-gate, bottom-contact OTFTs. The main reason is that bottom-contact OTFTs typically exhibit a larger potential drop due to poor contact between the semiconductor and source/drain electrodes. Nevertheless, bottom-gate, bottom contact OTFTs also demonstrate several positive sides. For example, the pre-patterned substrate with gold electrodes greatly reduces the device fabrication time. And the pre-patterned gold electrodes can be surface-treated, which could alter the workfunction of the electrodes to facilitate charge injection from source to organic semiconductor.

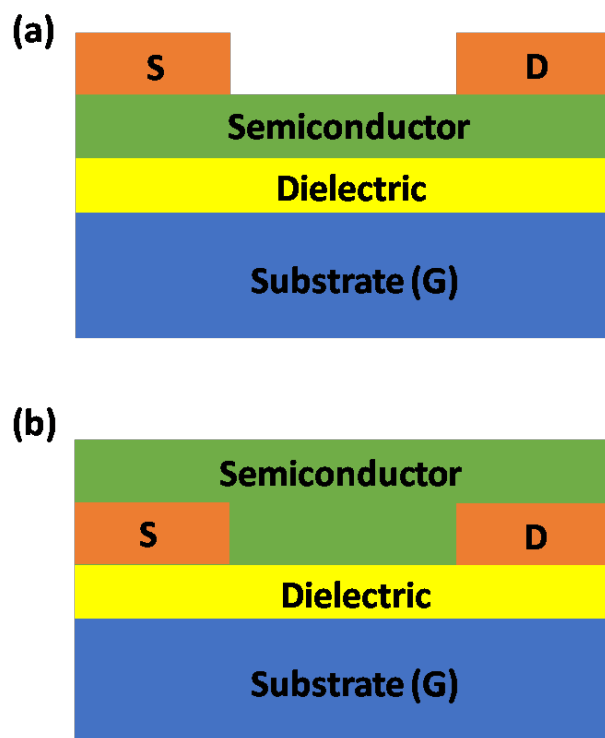


Figure 1.3 (a) bottom-gate, top-contact OTFT configuration, and (b) bottom-gate, bottom-contact OTFT configuration.

1.3 Organic Polymer Solar Cells (PSCs)

1.3.1 Introduction to Organic Polymer Solar Cells

Renewable and low-cost energy sources have gained increased attention as the traditional energy sources such as fossil fuel could be eventually used up thereby intensifying future energy crisis. Also greenhouse effect from such energy source starts threatening the human life. Among alternative sources of energy, including hydroelectric energy, wind energy and geothermal energy, solar energy is inexhaustible and always available for usage. The large magnitude of solar energy available makes it a highly appealing source of electricity. It is reported that only less than 0.02% of sun power reaches the earth but it is several times larger than the total world

energy consumption. Since the annual solar radiation from the sun produces significantly more energy than that consumed by the entire world's population in a year, much research has been invested in photovoltaic to harvest the sun's energy.

Nowadays, the mostly used solar cell is silicon solar cell, which uses silicon as absorbing material to harvest sunlight for photovoltaic conversion of electricity.

Organic solar cells, particularly solution processable polymer solar cells have attracted worldwide attention for the low-cost manufacture on flexible substrates. Currently their efficiency has reached to over 10%. Organic polymer materials are expected to be cheaper in mass production as compared with inorganic counterparts. Also most of the organic semiconducting materials can be dissolved in organic solvents, which makes solution processing possible. Solution processing at low temperature can greatly reduce fabrication cost which means organic solar cells can be fabricated on large, flexible substrates by roll-to-roll (R2R) printing like mass production of newspaper. Therefore, solution processable organic polymer solar cells have a great potential to be widely used in our daily life, particularly flexible electronics. In order to compete with their inorganic counterparts for a niche markets, organic solar cells have to improve their performance at higher efficiency levels. The current challenges of the organic photovoltaic mainly lie in the development of new donor and acceptor materials with better energy level alignment. In addition, the improvement of the transport properties of the materials through better control of the morphology and crystallinity are also pursued.

There are various organic solar cell structures. Single layer organic photovoltaic cell is the simplest one, in which organic electronic material is sandwich between two electrodes, as shown in Figure 1.4(a). When organic layer absorbs light, electrons and holes will be generated at the LUMO and HOMO energy level. The generated electron and hole charge carriers transport

between molecules by hopping, and finally reaches cathode and anode due to energy preference between organic semiconductor and electrode. Although single layer organic solar cell works, the power-conversion efficiency is very low. Following single layer organic solar cell structure, a more complex type of bilayer organic photovoltaic cell was developed as shown in Figure 1.4(b). It consists of two layers, electron donor and electron acceptor, between electrodes. Such structure is able to split generated electron-hole pairs (excitons) more efficiently. Bulk heterojunction is the most popular and efficient structure for polymer solar cells, as shown in Figure 1.4(c). In bulk heterojunction structure donor and acceptor materials are blended together as active layer. With optimization of processing conditions, the donor and acceptor molecules will self-assemble into an interpenetrating nanoscale network. The interpenetrating nanoscale donor and acceptor domains increase contact area and allows excitons that have short lifetime to reach the donor/acceptor interfaces for efficient dissociation and harvesting. Organic solar cells with bulk heterojunction structure have demonstrated the highest efficiency so far.

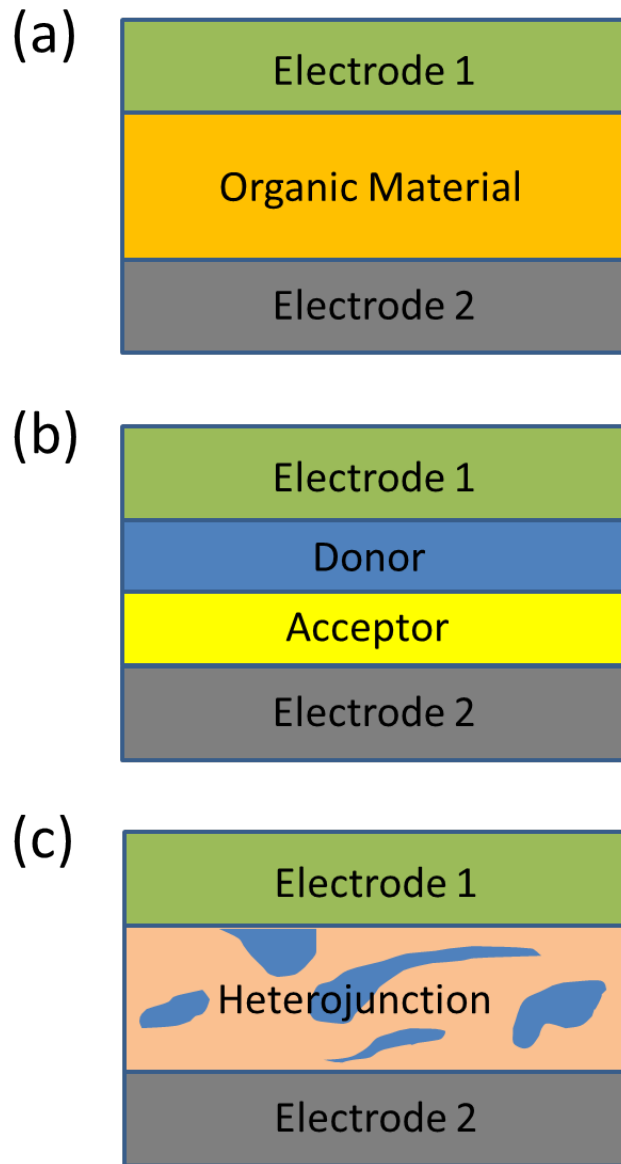


Figure 1.4 Sketch of (a) single layer, (b) bilayer, (c) bulk heterojunction polymer solar cell structures.

1.3.2 Operational Mechanism of Bulk Heterojunction Solar Cells and Architectures

Bulk heterojunction (BHJ) organic solar cells are comprised of a stack of layers, including active layer of a mixture of acceptor and donor materials, electron transport layer (ETL), hole transport layer (HTL). Active layer absorbs light and generate free charge carriers,

while ETL and HTL buffer layers ensure selective transport of free carriers. All these layers are sandwiched between two electrodes, ITO and metal layer. ITO electrode is transparent on glass or flexible substrate for sunlight illumination of the cell.

There are several steps to convert sun light energy to electricity in organic photovoltaics (OPVs). Sunlights with photon energy greater than HOMO-LUMO gap are first absorbed by active layer. Electrons are excited from HOMO to LUMO energy level, leaving holes in HOMO of donor polymer. Then, the generated electron/hole pairs (also called excitons) diffuse to the interface of donor and acceptor, and separated into free electrons and holes, as shown in Figure 1.5(a). After exciton dissociation, energy band diagram has to be resorted for the charge movement. As shown in Figure 1.5(b), generated electrons on the LUMO of donor move to the LUMO of acceptor and are collected at cathode, while generated holes transport in the donor and are collected at the anode. Holes could not transport to the HOMO level of acceptor because of the energy barrier. Finally, electricity as an electrical potential will be generated when negative electrons are accumulated at cathode and hole reaches anode.

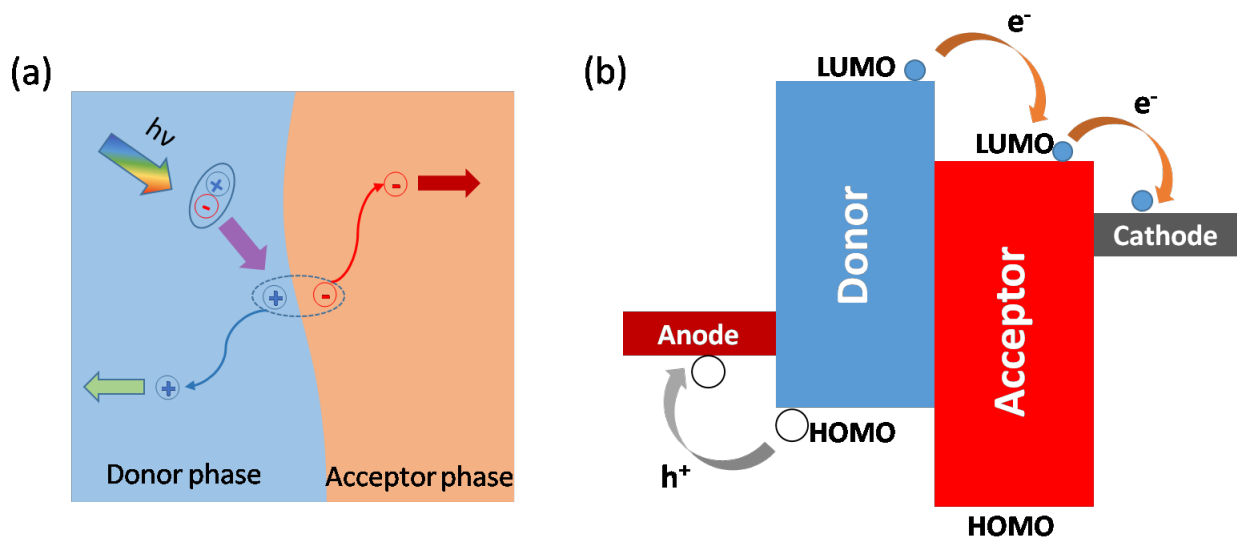


Figure 1.5 Schematics of (a) exciton generation/dissociation and charge transport , and(b) energy band diagram in organic polymer solar cells.

Depending on the direction of charge carrier transportation, Organic polymer solar cells with bulk heterojunction can be made into two kinds of configurations, regular structure and inverted structure, as shown in Figure 1.6. In regular structure, ITO on the glass substrate collects holes and serves as anode. The conducting polymer PEDOT:PSS on the top of ITO acts as hole transport layer. Electrons move up to Al cathode because of its low work function nature. In inverted structure, ZnO is deposited on the ITO glass, serving as electron transport layer for electron collection at ITO cathode. MoO₃ on the top of active layer act as hole transport layer. High work function metals, such as Ag or Au could be deposited on the MoO₃ hole transport layer as anode. Electrons and holes transport to the opposite direction as what it is in regular structure. In addition, regular structure normally gives a relatively higher efficiency but the device is unstable, sometimes devices could only last less than one day. On the other hand, inverted structure has a much better stability, which can last for several days with only a tiny degradation.

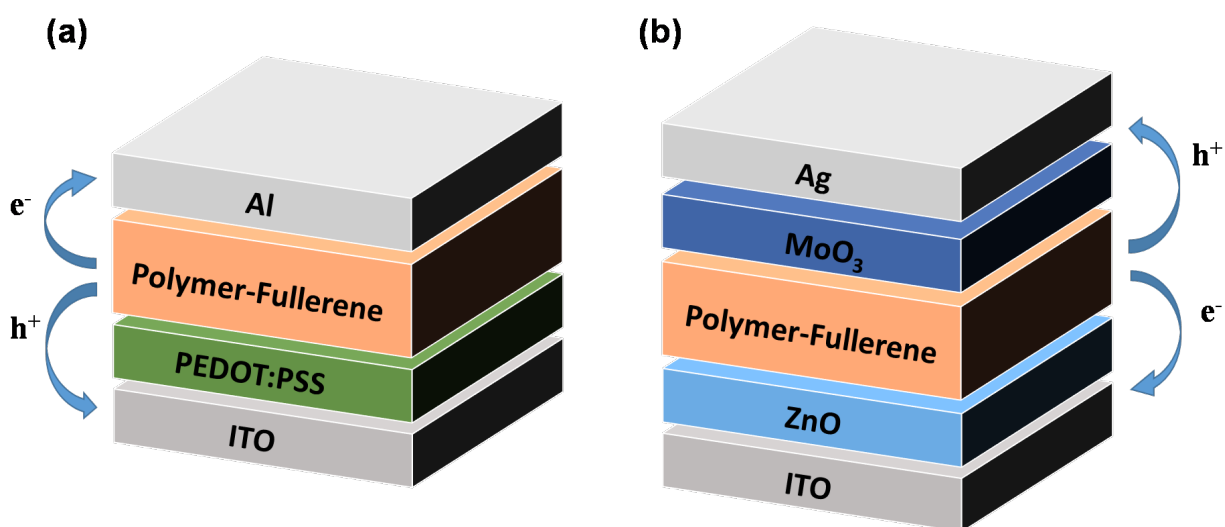


Figure 1.6 Configurations of polymer solar cells: (a) regular structure, and (b) inverted structure.

CHAPTER 2

SOLUTION-GROWN SMALL-MOLECULE ORGANIC SEMICONDUCTOR WITH ENHANCED CRYSTAL ALIGNMENT AND AREAL COVERAGE FOR ORGANIC THIN FILM TRANSISTORS

2.1 Introduction

Solution processable small-molecule organic semiconductors have been intensively studied nowadays due to their relatively high charge carrier transport,²³⁻²⁶ and cost-effectiveness in fabrication, which make them promising for applications in flexible electronics over large areas.²⁷⁻²⁹ However, thin films drop casted from small-molecule organic semiconductors typically exhibit random crystal orientation with poor coverage, which leads to significant performance variations of organic thin-film transistors (OTFTs).^{30, 31} Therefore, it is mandatory to well align the crystals in order to achieve performance consistency of OTFTs. Various efforts have been made to address these issues in different semiconducting material systems.³²⁻³⁴ For example, Lee et al. demonstrated the growth of 6,13-bis(triisopropylsilylethynyl)pentacene (TIPS pentacene) on a slightly tilted substrate, resulting in an array of ribbon-shaped TIPS pentacene crystals well-aligned in the tilted direction of the substrate.³⁵ More recently, Li et al. employed a “droplet-pinned crystallization” method to control the crystal growth of C60, which successfully leads to well-aligned C60 single crystals.³⁶ Nevertheless, the films obtained in all these work above still show low areal coverage, which must be improved in order to fabricate high-mobility OTFTs with performance uniformity.

In this work, we combine the “controlled evaporative self-assembly (CESA)” method³⁷⁻³⁹ with double solvent scheme^{40,41} to both control the crystal growth and enhance areal coverage of organic semiconductors. Since diketopyrrolopyrrole (DPP) based organic materials have attracted enormous interests for applications in both organic photovoltaics (OPV) and OTFTs, a derivative of DPP, 2,5-Di-(2-ethylhexyl)-3,6-bis(5"-n-hexyl-2,2',5',2"']terthiophen-5-yl)-pyrrolo[3,4-c]pyrrole-1,4-dione (SMDPPEH),⁴²⁻⁴⁹ is used as an example to demonstrate the effectiveness of our approach. When drop casted from single solvent (chloroform), SMDPPEH formed crystals with significant misorientation and poor film coverage. In comparison, the application of CESA method combined with double solvent system leads to greatly enhanced crystal alignment, film coverage and crystal width. As a result, the SMDPPEH OTFTs based on CESA approach and double solvent system exhibit a mobility of up to $1.6 \times 10^{-2} \text{ cm}^2/\text{Vs}$. To the best of our knowledge, this is the highest mobility from SMDPPEH ever reported.

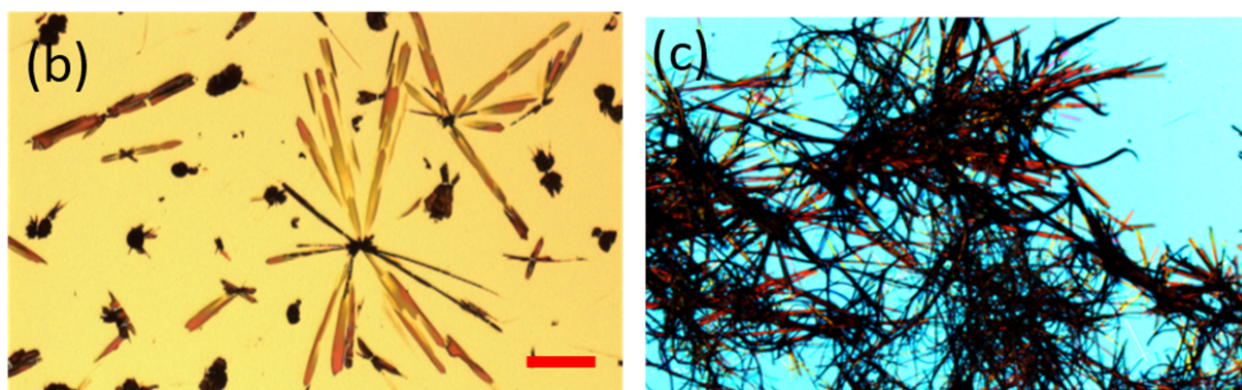
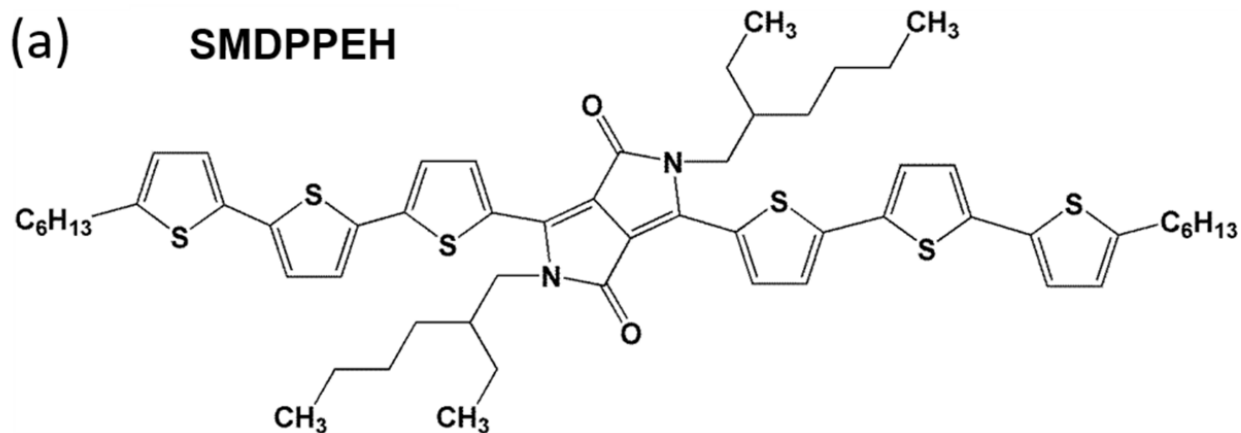


Figure 2.1.(a) Molecular structure of SMDPPEH. Optical image of SMDPPEH crystals drop casted in (b) single chloroform solvent and (c) chloroform/ethanol (5:1) double solvents. Figure (b) and (c) share the same scale bar of 100 μm .

2.2 Experiment

SMDPPEH material was purchased from Sigma Aldrich and used as received. Bottom-gate, bottom-contact transistors were fabricated on heavily doped n-type silicon substrates with a 100 nm thickness of thermally grown SiO_2 layer. The gold electrodes were patterned by using standard photolithography followed by metal deposition and lift-off. The patterned substrates with Au source/drain contacts were cleaned by acetone and isopropyl alcohol sequentially. Then surface treatments, including hexamethyldisilazane (HMDS) and pentafluorobenzenethiol

(PFBT) treatments, were carried out. HMDS treatment was utilized to passivate the silanol groups on the hydrophilic SiO₂ substrate surface, whereas PFBT treatment was performed to tune the energy level of gold contacts for facilitating hole charge injection.⁵⁰ Specifically, HMDS self-assembled monolayers were formed on the gate dielectric via vapor deposition at 140 °C, and rinsed off the residue of HMDS by isopropyl alcohol. PFBT treatment was performed on the source/drain gold contacts by immersing the substrates in a 10mM PFBT/toluene solution for 2 hours, followed by rinsing with toluene.

SMDPPEH in chloroform/ethanol double solvents (3 mg/ml) was drop casted onto the substrate to form an active layer. In the double solvent system, chloroform was selected as the “good” solvent since SMDPPEH can be well dissolved in chloroform, whereas ethanol was used as the “bad” solvent because of the limited solubility of SMDPPEH in ethanol. Moreover, the similarity of the boiling points between ethanol (78.4°C) and chloroform (61.2°C) ensures simultaneous evaporation when the CESA method is applied for crystal alignment. If there exists a big difference in boiling point between “good” and “bad” solvent, the solution will eventually ends up with one single solvent situation. Optical micrographs of SMDPPEH thin film were taken by using a Zeiss Axioplan optical microscope with a build-in camera. Current-voltage (I – V) characteristics were carried out with an Agilent B1500A semiconductor parameter analyzer. Each device was measured three times to ensure the consistency of results. All measurements were performed in ambient environment at room temperature. Field-effect mobilities in the saturation regime were extracted from the slope of the $(I_{DS})^{1/2} - V_{GS}$ transfer characteristic.

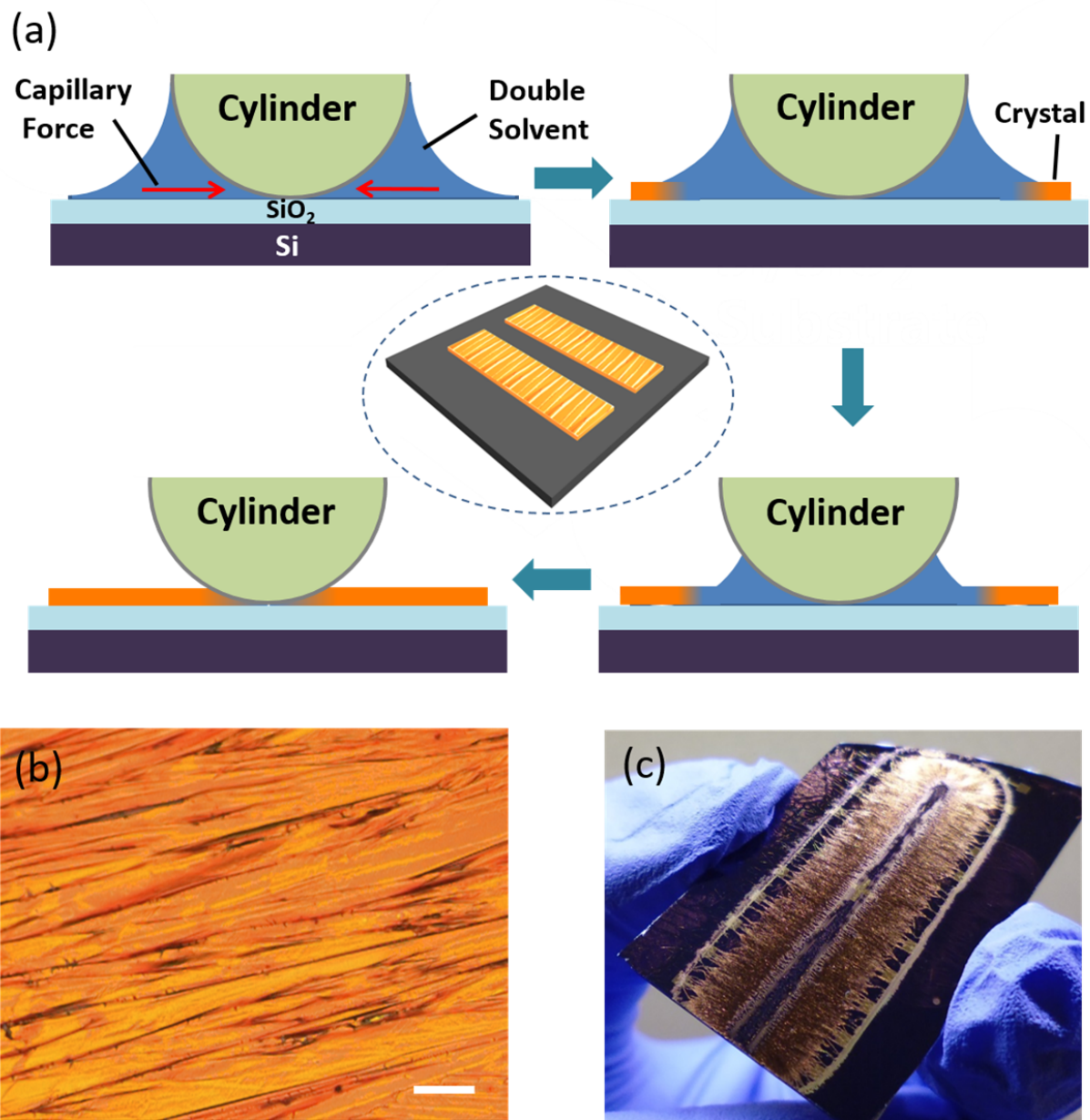


Figure 2.2.(a) Schematic of the CESA method for crystal alignment. (b) The zoom in optical image of SMDPPEH films with highly orientated crystals and great film coverage. The scale bar represents 50 μm . (c) digital image of crystal growth over entire substrate with chloroform/ethanol ratio of 5:1.

2.3 Results and Discussion

DPP is best known for its ease of side-chain substitution which forms different functional groups and leads to a good field-effect mobility.⁵¹⁻⁵³ As a newly-developed derivative of DPP, SMDPPEH hosts two pendant alkyl chains, which increases its solubility and thermal stability.⁵⁴ The molecular structure of SMDPPEH is shown in Figure 2.1(a). When SMDPPEH is drop casted from single chloroform solvent, a few scattered crystals are formed on the substrate with random orientation and poor areal coverage (Figure 2.1(b)), while drop casted from chloroform/ethanol double solvents, the resultant films exhibit enhanced crystal density as shown in the optical images of Figure 2.1(c), because the “bad” solvent ethanol increases nucleation seeds for SMDPPEH crystallization. In both cases of crystal growth in single and double solvents, however, there is no uniform crystal orientation, which could cause significant device performance variation if such films are used as the active layer of OTFTs.^{55,56} In order to address these issues, we applied the CESA method combined with the double solvent system to effectively control the crystallization, and obtained SMDPPEH crystalline films with enhanced crystal alignment and areal coverage.

The CESA method applied to effectively align the SMDPPEH crystals is illustrated in Figure 2.2(a). As shown in the schematic, SMDPPEH solution was constrained in the cylinder-on-flat geometry, due to the capillary force between the cylinder and the substrate. When the contact line of the solution is pinned during solvent evaporation, the edge of the droplet has a higher evaporation rate which leads to elevated solution concentration.⁵⁷ This further facilitates an outward flow carrying more solutes from the droplet center to the periphery,⁵⁸ where nucleation seeds are formed from the solutes. When the solution reaches supersaturation, SMDPPEH molecules start to crystallize from the nucleation seeds and grow along the direction

of capillary force towards the contact center between the cylinder and the substrate. With the combination of CESA method and double solvent system, well-aligned SMDPPEH crystals with significantly improved film coverage were achieved, as shown in the optical images of Figure 2.2(b). The digital image of Figure 2.3(c) shows the crystal growth over the entire substrate. The chloroform/ethanol double solvent is at 5:1 ratio.

In order to optimize the SMDPPEH film morphology with CESA method, different ratios between “good” solvent chloroform and “bad” solvent ethanol were tested. When a small amount of ethanol was added as in the case of chloroform/ethanol at 15:1 ratio, a few SMDPPEH crystals with enhanced crystal width and orientation were formed because only a small number of nucleation seeds from “bad” solvent ethanol were generated at this ratio, whereas the majority of the SMDPPEH material directly precipitated or formed many small crystals onto the substrate as round-shaped crystal aggregations as shown in Figure 2.3(a). When the amount of ethanol increased to chloroform/ethanol ratio of 10:1 and 5:1, both crystal orientation and coverage of the SMDPPEH film were improved (Figure 2.3(b) and (c)). Particularly, chloroform/ethanol at 5:1 ratio leads to the most improvement in the thin-film morphology of SMDPPEH, in terms of the best crystal alignment, the highest film coverage and the largest crystal width. However, if the amount of ethanol further increased to 1:1 (Figure 2.3(d)), both crystal width and film coverage of the SMDPPEH film decreased dramatically and crystal misorientation started to appear. Finally, the CESA method lost control of SMDPPEH crystal alignment when the amount of ethanol increased to chloroform/ethanol at 1:5 ratio, and the resultant film exhibited significant crystal misorientation with large gaps in between (Figure 2.3(e)).

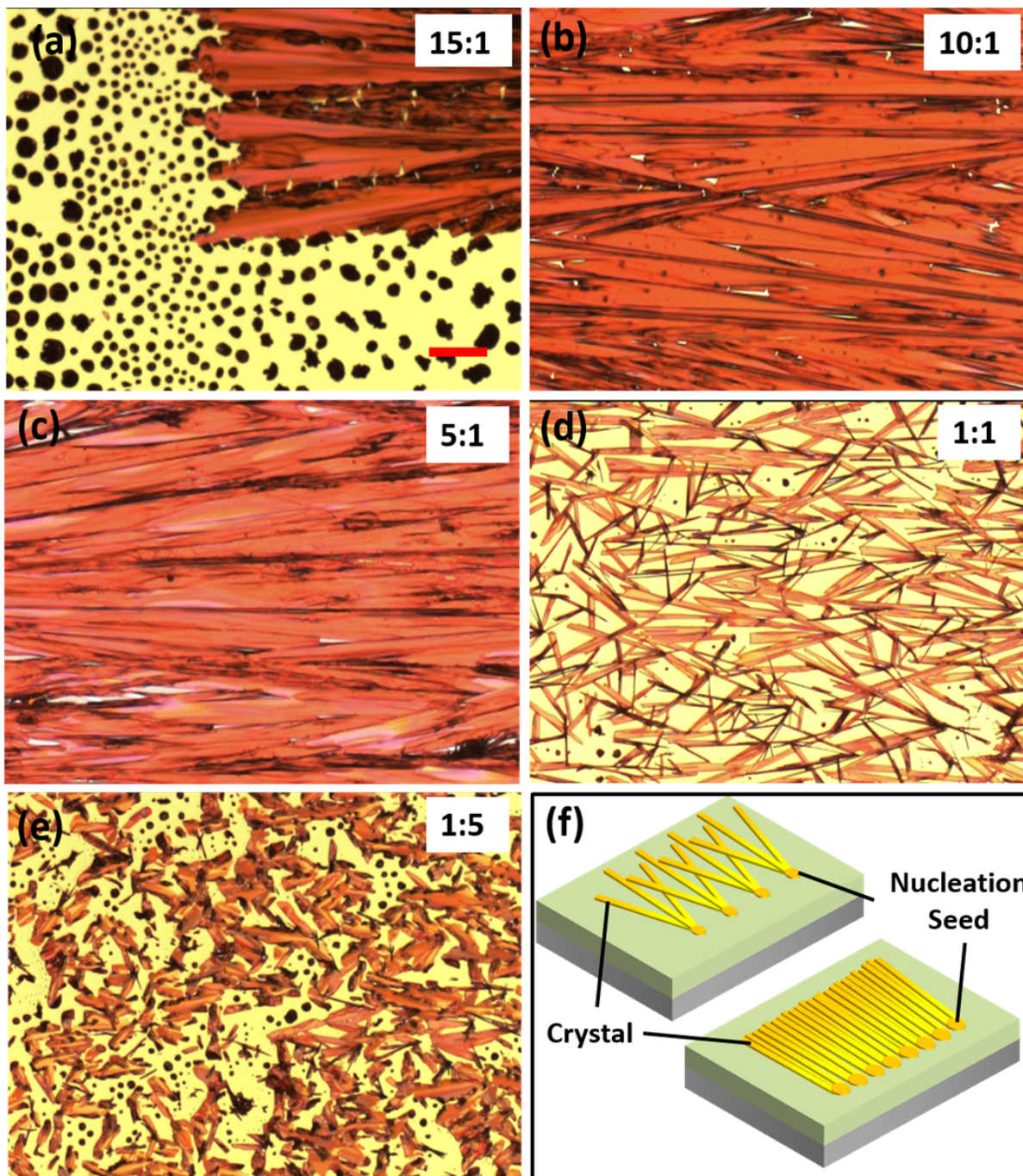


Figure 2.3. Optical micrographs of SMDPPEH crystals drop casted from chloroform/ethanol double solvents at different ratios: (a) 15:1, (b) 10:1, (c) 5:1, (d) 1:1 and (e) 1:5, respectively. All images share the same scale bar of $100\mu\text{m}$ as shown in (a). (f) Effect of nucleation seed density on crystallization.

The change in the crystal orientation, areal coverage and crystal width of the SMDPPEH film can be reasonably explained by the intermolecular interaction between SMDPPEH and ethanol. When the ethanol solvent is added, it is expected that the hydroxyl groups in ethanol facilitate the intermolecular π - π overlapping of SMDPPEH backbones, further leading to the supramolecular aggregation of SMDPPEH molecules that serve as nucleation seeds.⁵⁹ When the solution supersaturation point is reached, the SMDPPEH molecules start to crystallize from the nucleation seeds and grow in the same direction as of the capillary force, resulting in well-aligned SMDPPEH crystals with enhanced crystal coverage and width. In specific, when a small amount of ethanol is added as in the case of chloroform and ethanol at 15:1 ratio, the slight supramolecular aggregation of SMDPPEH molecules created only a small number of nucleation seeds, contributing to the formation of a few well-aligned crystals, as illustrated in the top left cartoon of Figure 2.3(f). Nevertheless, the majority of the SMDPPEH material directly precipitated or formed many small crystals onto the substrate as round-shaped aggregations. When the ratio between chloroform and ethanol changes to 10:1 and 5:1, more addition of ethanol provided more hydroxyl groups and simultaneously increased both the nucleation seed number and density, which significantly enhances crystal width and film areal coverage while at the same time further improving the crystal alignment as illustrated in the bottom right cartoon of Figure 2.3(f). However, when the ratios between chloroform and ethanol further change to 1:1 and 1:5, it is likely that the excessive amount of ethanol would consume most of the SMDPPEH for the formation of nucleation seeds, so very few SMDPPEH solutes were dissolved in the solution as supply for crystallization, consequently leading to the formation of many small crystals with significantly reduced crystal width, areal coverage and crystal orientation.

To more accurately demonstrate the effect of different double solvent ratios on the SMDPPEH thin film morphology, the average misorientation angle, crystal coverage and width were quantitatively characterized, as shown in Figure 2.4. The standard deviation of misorientation angle is based on 10 crystals for each type of film, whereas that of the crystal width is based on 14 crystals. The direction of capillary force is chosen as the baseline, and misorientation angle is defined as the angle between the long axis of a crystal ribbons and the baseline. The SMDPPEH film drop casted from chloroform/ethanol double solvent at the 15:1 ratio shows an average misorientation angle of $6\pm 5^\circ$, indicating the addition of a small amount of ethanol can largely reduce the crystal misorientation. The misorientation angle further reduces to $4\pm 3^\circ$ and $4\pm 2^\circ$ when the ethanol amount reaches to the 10:1 and 5:1 ratios, respectively, which demonstrates the SMDPPEH crystals are well-orientated. However, further increasing the ethanol amount to the 1:1 and 1:5 ratios would cause the misorientation angle to increase to $11\pm 7^\circ$ and $30\pm 20^\circ$, respectively.

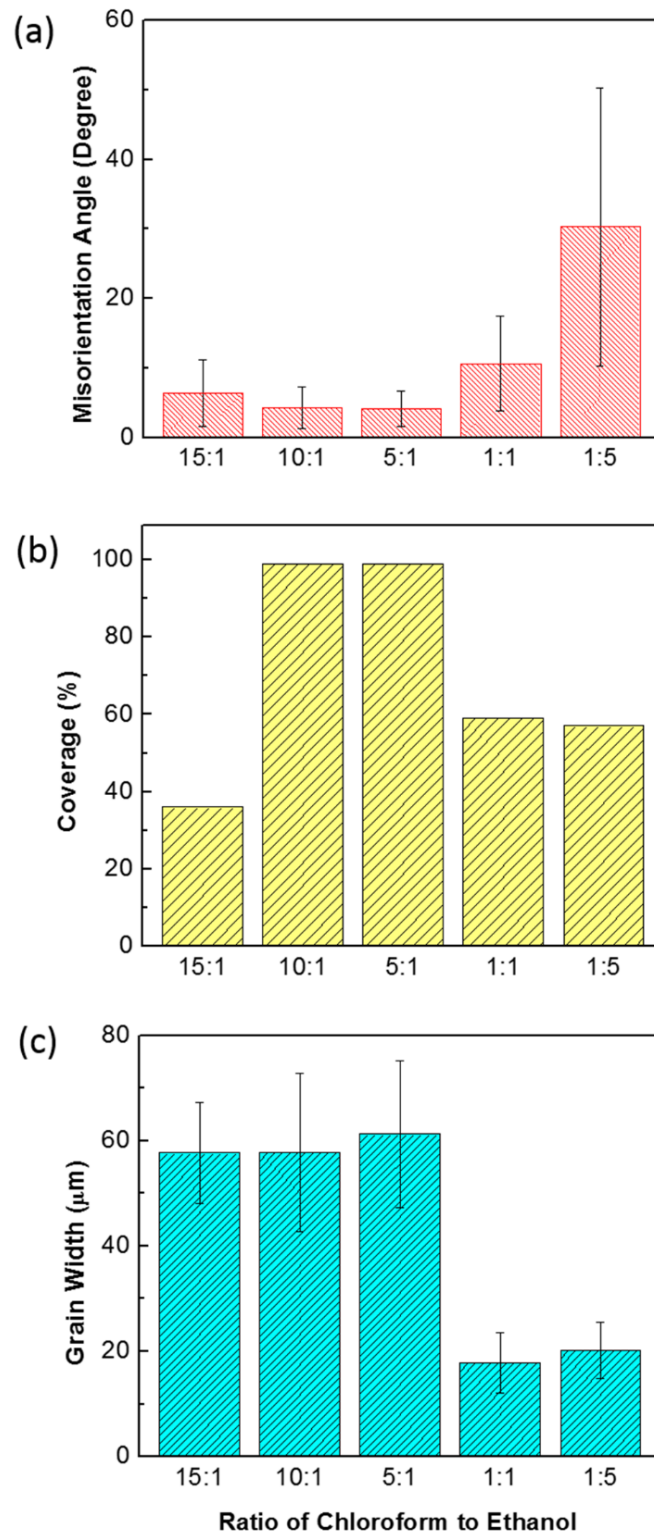


Figure 2.4. Quantitative analysis of the (a) average crystal misorientation, (b) film coverage, and (c) average crystal width of the SMDPPEH crystals at different ratios of the chloroform/ethanol double solvents.

The areal coverage of the SMDPPEH films at different double solvent ratios was plotted in Figure 2.4(b). At chloroform/ethanol 15:1 ratio, the film has areal coverage of ~36%, which is enhanced to ~99% when the addition of ethanol increases to both 10:1 and 5:1 ratios, implying that the CESA method with optimal double solvent ratio can not only effectively align the crystal growth, but also reduce the crystal gaps and enhance the film coverage. When the ethanol is further increased to 1:1 and 1:5 ratios, the areal coverage decreased to ~59% and ~57%, respectively. Moreover, the average crystal width of SMDPPEH films was also quantitatively calculated based on the optical microscope images and was plotted in Figure 2.4(c). The SMDPPEH film at chloroform/ethanol 15:1 ratio exhibits an average crystal width of $58 \pm 10 \mu\text{m}$, whereas those films at 10:1 and 5:1 ratios show an average crystal width of $58 \pm 15 \mu\text{m}$ and $61 \pm 14 \mu\text{m}$, respectively. In particular, the chloroform/ethanol 5:1 leads to the largest crystal width. When the solvent volume ratio further changes to 1:1 and 1:5, the average crystal width is reduced to $18 \pm 6 \mu\text{m}$ and $20 \pm 5 \mu\text{m}$, respectively.

Bottom-gate, bottom-contact OTFTs were fabricated, and the device configuration with SMDPPEH microribbons as active semiconducting layer is illustrated in Figure 2.5(a). From the slope of the square root plot $(I_{DS})^{1/2} - V_{GS}$ in the transfer characteristic (Figure 2.5(b)), the field-effect mobility in the saturation region was extracted to be $1.6 \times 10^{-2} \text{ cm}^2/\text{Vs}$ by using the following traditional MOSFET equation:

$$I_{DS} = \left(\frac{WC_i\mu_{sat}}{2L} \right) (V_{GS} - V_T)^2 \quad (1)$$

where W is the effective channel width based on the actual crystal coverage in the channel region, L is the channel length, C_i is the capacitance per unit area of the gate insulator, μ_{sat} is the field-effect mobility in the saturated region, V_{GS} is the gate voltage and V_T is the

threshold voltage. To the best of our knowledge, this is the highest mobility ever reported from the solution-processed SMDPPEH semiconductor. Moreover, our mobility is much larger than the value of other p-type semiconductors commonly studied as the donor materials of photovoltaic cells, such as poly(3-hexylthiophene-2,5-diyl) (P3HT),³⁸ indicating SMDPPEH is a promising donor material for solution-processed solar cells. In addition to the field-effect mobility, the threshold voltage V_T was extracted to be -4V, and the current on/off ratio $I_{on/off}$ is 4.3×10^4 .

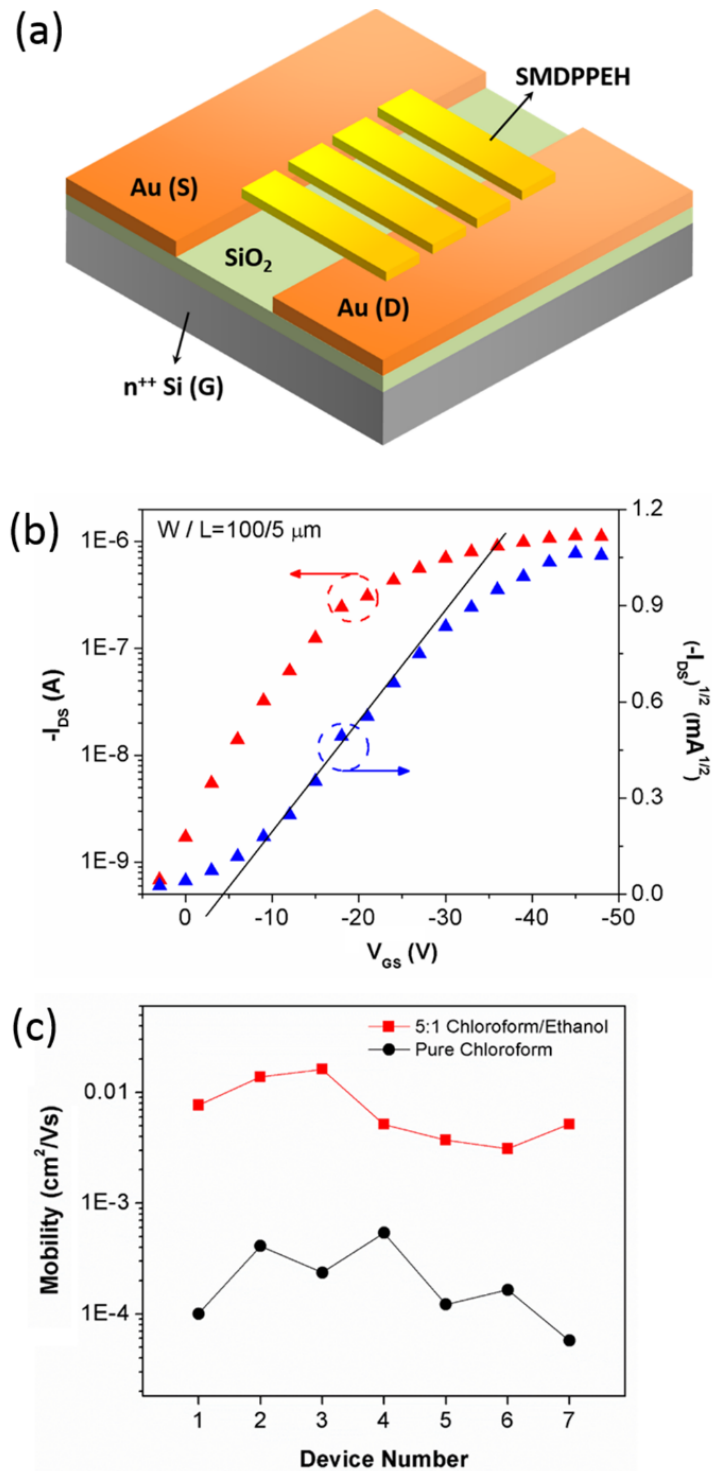


Figure 2.5. (a) Schematic of bottom-gate, bottom-contact OTFTs with SMDPPEH crystal ribbons as active layer. (b) Transfer characteristics for field-effect mobility extraction. The volume ratio of chloroform to ethanol solvent is 5:1. (c) Mobility variation of SMDPPEH OTFTs based on different types of films.

Finally, we plotted the OTFT mobilities against different types of films as shown in Figure 2.5(c). The mobilities of SMDPPEH OTFTs drop casted from pure chloroform without applying the CESA method varied from $5.7 \times 10^{-5} \text{ cm}^2/\text{Vs}$ to $5.4 \times 10^{-4} \text{ cm}^2/\text{Vs}$, with an average mobility of $2.3 \times 10^{-4} \pm 1.8 \times 10^{-4} \text{ cm}^2/\text{Vs}$. In comparison, the devices made from 5:1 chloroform/ethanol double solvents with the CESA method demonstrated hole mobilities which ranged from $3.1 \times 10^{-3} \text{ cm}^2/\text{Vs}$ to $1.6 \times 10^{-2} \text{ cm}^2/\text{Vs}$, with an average mobility of $7.8 \times 10^{-3} \pm 5.1 \times 10^{-3} \text{ cm}^2/\text{Vs}$. The results above demonstrated that the combination of CESA method and double solvent system effectively improves the charge transport and significantly enhances the average mobility of SMDPPEH OTFTs.

2.4 Crystal Alignment by Interaction Between SMDPPEH Small Molecule and P3HT Conjugated Polymer

In addition to the crystal alignment through combined CESA method and double solvent approach, addition of conjugated polymer P3HT was also tried to align SMDPPEH crystals. Both SMDPPEH and P3HT materials were purchased from Sigma Aldrich and used as received. Bottom-gate, top-contact transistors were fabricated on heavily doped n-type silicon substrates with a 300nm thickness of thermally grown SiO₂ layer. The Si/SiO₂ substrates were cleaned by acetone and isopropyl alcohol for 30 minutes sequentially followed by octadecyltrichlorosilane (OTS) treatment to passivate the silanol groups on the hydrophilic SiO₂ surface. Then the substrate was immersed in hexadecane for 10 minutes followed by rinsing in hexane and IPA. Finally, substrate was blow dried by nitrogen.

SMDPPEH and P3HT with different ratios were first dissolved in chloroform. Then the solution was treated at 50°C on hot plate for 10 minutes followed by ultrasonic agitation for 6

minutes. Various concentration of solution was drop casted onto the pre-cleaned substrate to form an active layer. During the crystal growth, 0.5ml of chloroform was dropped around the substrate in petri dish for solvent vapor annealing. Finally, 50nm of gold was thermally evaporated on top of the film through shadow mask at the rate of 1Å/s. Current-voltage ($I-V$) characteristics were done with an Agilent B1500A semiconductor parameter analyzer. Each device was measured three times to ensure the consistency of results. All measurements were performed in ambient environment at room temperature. Field-effect mobilities in the saturation regime were extracted from the slope of the $(I_{DS})^{1/2} - V_{GS}$ transfer characteristic. Optical micrographs of SMDPPEH thin film were taken by using a Zeiss Axioplan optical microscope with a build-in camera.

The morphologies of slowly crystallized SMDPPEH and P3HT blends are shown in Figure 2.6. Figure 2.6(a)-(c) present optical micrographs of the two components at different ratios with a concentration of 2mg/ml. The morphology has a huge variation with the change of SMDPPEH to P3HT ratios. At the weight ratio of 1:1, SMDPPEH crystals are small without any orientations because the large amount of P3HT polymers tend to aggregate to form a thick film and prevent SMDPPEH crystals from growing wider and longer. When the SMDPPEH to P3HT ratio increased to 5:1, the SMDPPEH and P3HT blends forms grass-like, needle shaped crystals with improved orientation and alignment. These SMDPPEH crystals are growing toward almost the same direction. When further increases the concentration of SMDPPEH to 10:1, crystals tend to become narrower and shorter with less orientation. Also large numbers of cracks on crystals can be observed. These cracks will seriously reduce the charge transport in the crystals thereby degrading the performance of OTFTs.

Figure 2.6(d)-(f) show the morphologies of SMDPPEH and P3HT mixing solution at various concentrations with the optimal ratio of 5:1 between SMDPPEH and P3HT. With the concentration of 1mg/ml, the crystals are narrow with many cracks along the crystal. It is anticipated that when the concentration is too low, there are not enough materials for crystal growth to form a continuously nanowire. When the concentration reaches 2mg/ml, SMDPPEH crystal wires are perfectly grown and aligned. Low voltage SEM image was taken as shown in inset image. The needle crystals are formed with SMDPPEH in the middle and P3HT polymer around it. When the concentration reaches 5mg/ml, too much P3HT materials result in a thin film with very few SMDPPEH crystals on the top of it.

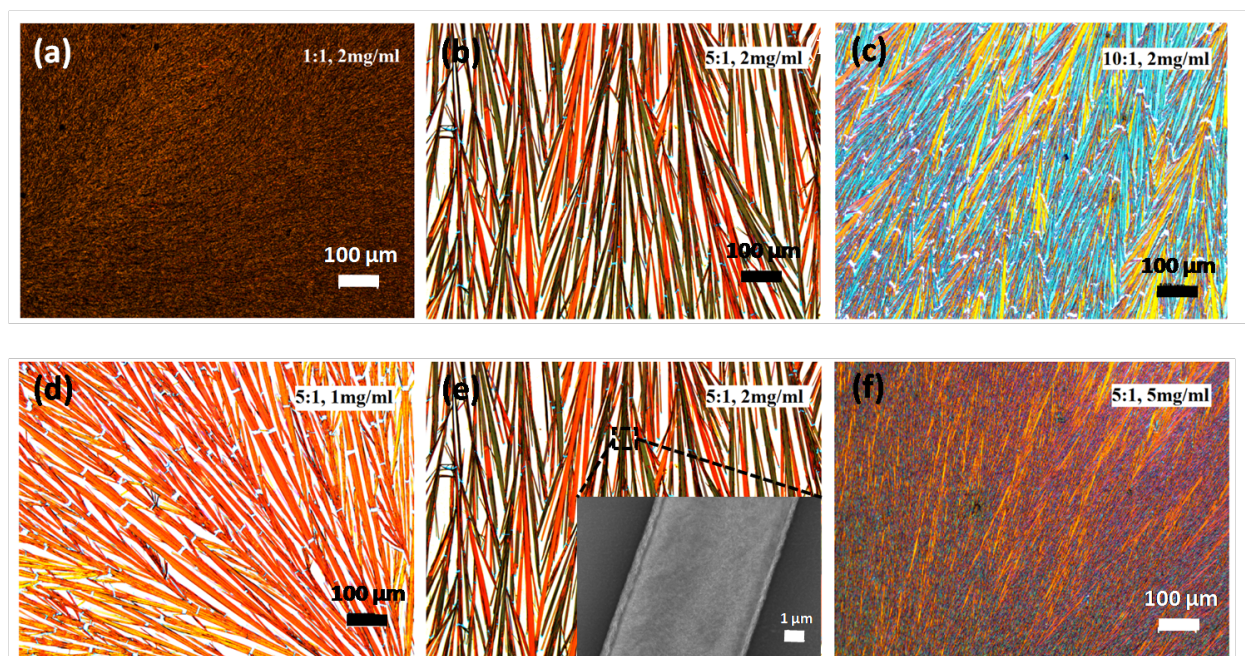


Figure 2.6 Optical images of SMDPPEH and P3HT blends at different ratios and concentrations. (a)-(c) Ratio of SMDPPEH to P3HT varies from 1:1 to 10:1 at the same concentration of 2mg/ml. (d)-(f) Different concentration of SMDPPEH and P3HT solution at the same ratio of 5:1. All optical images share the same scale bar.

After optimization of crystal growth with well-aligned SMDPPEH crystals, bottom-gate, top-contact OTFTs were fabricated and the device configuration with SMDPPEH and P3HT blend crystals as active semiconducting layer is illustrated in Figure 2.7(a). Figure 2.7(b) and (c) show the output and transfer characteristics from OTFTs based on SMDPPEH crystal ribbons. From the slope of the square root plot $(I_{DS})^{1/2} - V_{GS}$ in the transfer characteristic, the field-effect mobility in the saturation region was extracted to be $10^{-3} \text{ cm}^2/\text{Vs}$.

In addition to the field-effect mobility, the threshold voltage V_T was extracted to be -4V , and the current on/off ratio I_{on}/I_{off} is 4.3×10^4 .

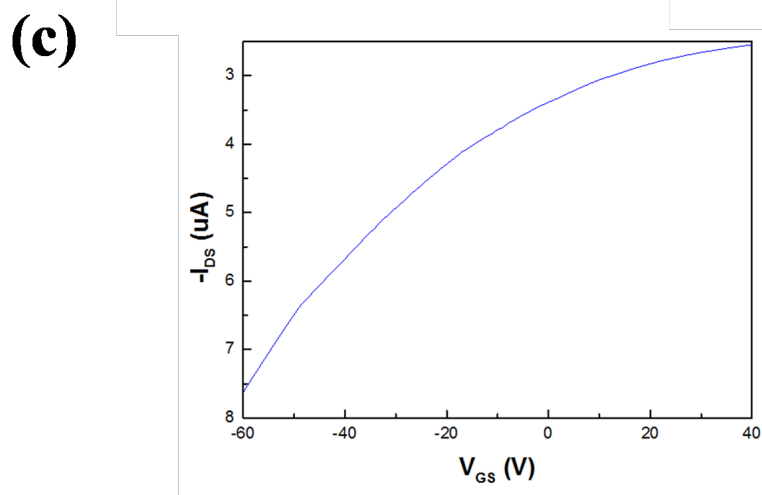
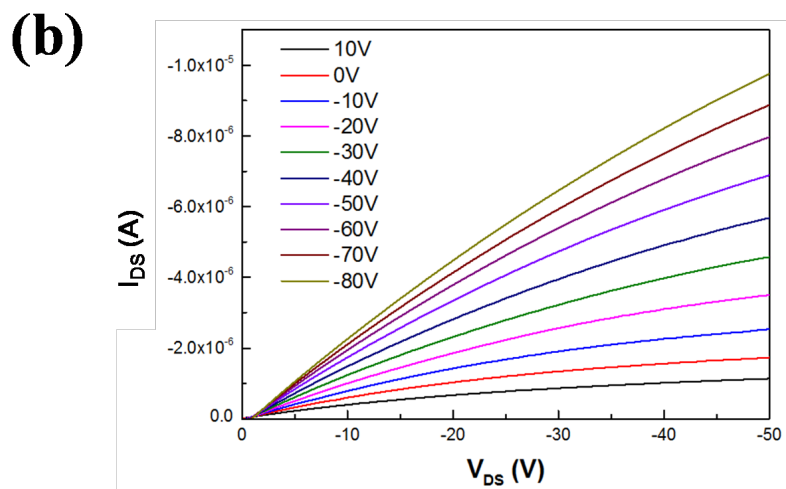
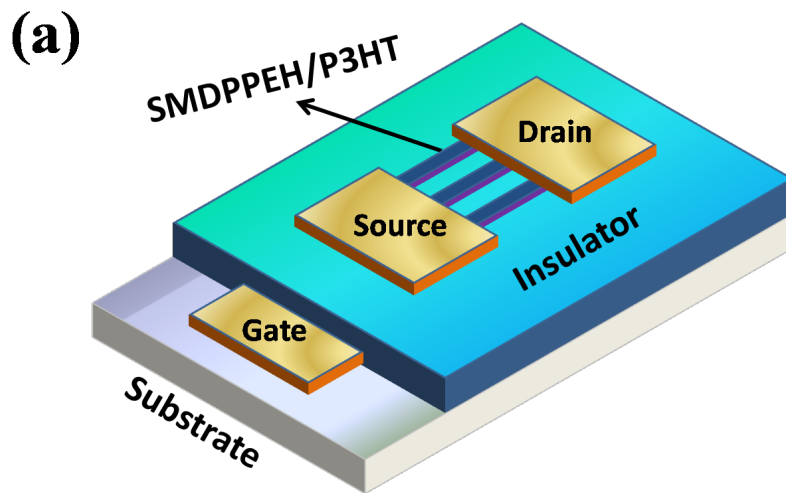


Figure 2.7(a) Schematic of bottom-gate, top-contact OTFTs with SMDPPEH and P3HT blend crystal ribbons as active layer. (b) Output and (c) transfer characteristics. The volume ratio of SMDPPEH to P3HT is 5:1 with the concentration of 2mg/ml.

2.5 Conclusion

In summary, the CESA method combined with the double solvent system is applied to achieve controlled crystallization of solution processable small-molecule organic semiconductors. Small molecule SMDPPEH is used as an example to demonstrate the effectiveness of the approach. The greatly enhanced crystal alignment, film coverage and crystal width have been achieved. The effect of different ratios between the chloroform/ethanol double solvents on crystal film morphology were investigated, and chloroform/ethanol at 5:1 volume ratio was found to lead to the optimal film morphology with the best crystal orientation, the highest film coverage and the largest crystal width. As a result, a mobility of $1.6 \times 10^{-2} \text{ cm}^2/\text{Vs}$ has been obtained, which is the highest mobility from solution-processed SMDPPEH OTFTs ever reported.

In addition, conjugated polymer, P3HT, was also used to help with SMDPPEH alignment. With optimized SMDPPEH to P3HT ratio of 5:1 and solution concentration of 2mg/ml, well-aligned SMDPPEH crystal wires were obtained. As a result, a mobility of $10^{-3} \text{ cm}^2/\text{Vs}$ from SMDPPEH crystal was achieved, which is 10 times higher than that reported in literature.

CHAPTER 3

INFLUENCE OF VERTICAL COMPOSITION PROFILE ON EFFICIENCY OF ORGANIC POLYMERIC SOLAR CELLS

3.1 Introduction

By showing great promise as a green, flexible and low-cost renewable energy sources, polymer-fullerene bulk heterojunction polymer solar cells (PSCs) have become the focus of attention worldwide.^{1-3, 60-64} In recent years the record efficiency has been frequently broken through.^{49, 65, 66} However, the research on the device optimization and fundamental understanding on the physical mechanisms is still on the way, as compared to the rapid progress made on power-conversion efficiency.

Morphology control is a key parameter for maximizing the effectiveness of donor-acceptor combinations on performance improvement. The blend morphology of electron-donating polymer and fullerene acceptor is complicated and sensitive to processing conditions. An impure phases, a hierarchy or broad distribution of domain sizes and a vertical composition gradient could be produced through solution processing. There has been substantial efforts to understand the morphology evolution in polymer-fullerene bulk heterojunction, particularly P3HT-PCBM system.⁶⁷⁻⁷⁰ It is well known that the lateral phase separation controls charge carrier dissociation and recombination at the polymer-fullerene interface, while the vertical distribution

of each phase in the blend film influences charge transport in the heterojunction and collection to the electrodes. With optimization of solution processing conditions, nanoscale interpenetrating donor-acceptor morphology could typically be obtained in the lateral direction. However, due to the sensitivity on environment and processing conditions, various P3HT-PCBM vertical composition profiles have been demonstrated. For example, Yang Yang's research group shows that the difference of surface energy and interactions between fullerene and substrate lead to a PCBM aggregation near ITO anode while P3HT stays close to cathode.⁷¹ On the other hand, van Bavel *et al* discovered an opposite vertical structure with P3HT tending to accumulate next to anode and PCBM close to cathode.⁷² Interestingly, another vertical configuration, i.e., sandwich structure, was reported by Z. Sun and his colleagues. In such sandwich vertical composition profile P3HT-rich layer were found in the middle of the active layer and sandwiched by PCBM-rich layers near both anode and cathode contacts.⁷³ The diverse distribution of P3HT and PCBM in the vertical direction results in various routes of charge carrier transportation and thus leading to a performance difference.

In this study, different P3HT-PCBM vertical configurations in active layer were established and systematically investigated for both regular and inverted PSC structures. P3HT-PCBM system is adopted as a benchmark since this donor-acceptor blend has been extensively studied and reported, which provides massive literature database for comparison. Semiconducting emissive thin film optical simulator (SETFOS)^{74, 75} from Fluxim AG is employed to create models with different vertical configurations and simulate the PSC performance. After comparing the performance of PSCs with different vertical configurations, we further studied the effect on open circuit voltage (V_{OC}), short circuit current (I_{SC}) and fill

factor (FF) and get the insight of the physical principle underlying from the view of charge carrier generation, transport and recombination.

3.2 Model Establishment and Simulation Parameters

As illustrated in Figure 3.1 (a-e), five different vertical configurations including sandwich I, sandwich II, charge transport favorable, charge transport unfavorable, and uniform structures are schematically established and described. Since electrons transport in PCBM and are collected at cathode and holes transport in P3HT and are collected at anode as indicated in bulk heterojunction energy band diagram in Figure 3.1(f), PCBM-rich layer close to cathode facilitates electron transport and collection, while P3HT-rich layer near anode benefits hole transportation and collection. In charge transport favorable structure the weight percentage of PCBM increases monotonically from ITO cathode side to Al cathode end as 20%, 40%, 60% and 80%, in which P3HT percentage decreases accordingly. The charge transport unfavorable structure possesses a completely reversed PCBM/P3HT distribution as compared to the favorable one. Through the charge transport unfavorable configuration, ratio of PCBM decreases continuously from 80% to 20% in the active layer, while concentration of P3HT increases from 20% to 80% accordingly from ITO anode side to the Al cathode end. Each constructing layer of various PCBM percentages has thickness of 20nm with total active layer thickness of 80nm.

There are two kinds of sandwich structures. In sandwich I configuration, a layer of 20% PCBM was introduced at the middle to represent the P3HT-rich layer, and the concentration of PCBM gradually increases toward both anode and cathode ends, i.e. 40% and 60% PCBM layers were placed outwards subsequently with 80% PCBM aggregation near the electrodes. The

sandwich II configuration follows an opposite distribution, in which 80% PCBM-rich layer is sandwiched by layers with gradually reduced PCBM percentage (60% PCBM layer followed by 40% PCBM layer in series) till intense P3HT aggregation layers at both ends of the active layer. For sandwich structure, the centered layer has thickness of 20nm, while the outer layers serving as the concentration gradient of PCBM have thickness of 10nm. As for uniform structure, 50% PCBM or P3HT is evenly distributed across the entire active layer. All the structures described above have total active layer thickness of 80nm. The thicknesses of Al, PEDOT:PSS and ITO are 100nm, 40nm, 120nm, respectively.

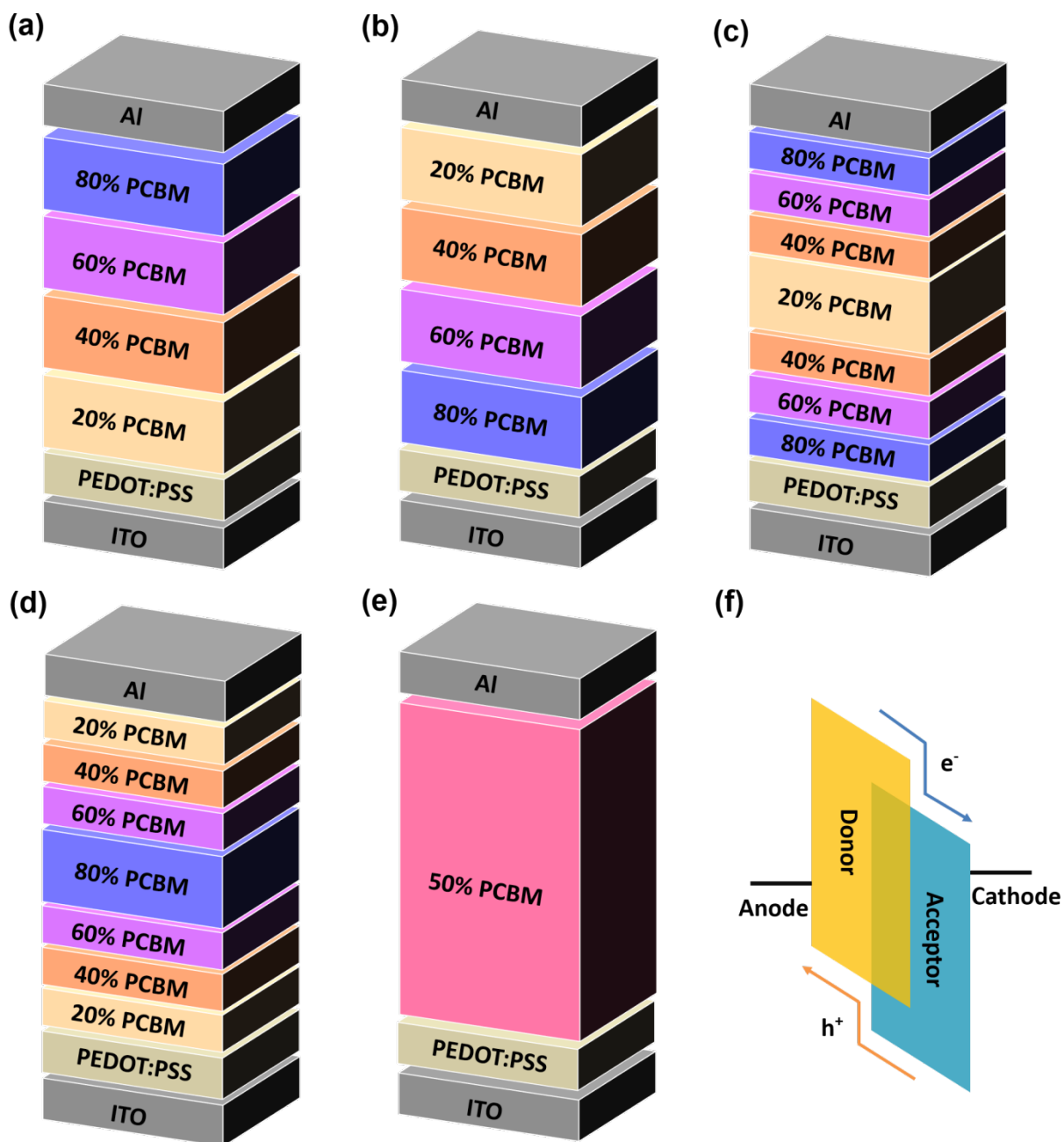


Figure 3.1. Schematic of the vertical composition profile of (a) sandwich I, (b) sandwich II, (c) charge transport favorable, (d) unfavorable, (e) uniform configuration of active layer in regular PSC structure, and (f) direction of charge carriers transport in the active layer.

In the device modeling, the work functions of ITO, PEDOT:PSS and Al are 4.3eV, 5.0eV and 4.3eV, respectively, which are used in most literatures as standard values. The dielectric constant for the active layer is 5.13. Other electronic parameters used in SETFOS modeling, including electron and hole mobility, charge generation efficiency, and Langevin recombination efficiency, are summarized in Table 3.1. All these electronic properties vary as a function of PCBM percentage. These input parameter values are taken based on literature reports with trend justified from material and device physics underneath.

Table 3.1. Electronic parameters of P3HT/PCBM blend at different PCBM percentages.

Parameter	20% PCBM	40% PCBM	50% PCBM	60% PCBM	80% PCBM
Electron mobility ($\text{cm}^2\text{V}^{-1}\text{s}^{-1}$)	7E-5	7E-4	1E-3	4E-3	3E-2
Hole mobility ($\text{cm}^2\text{V}^{-1}\text{s}^{-1}$)	4E-3	1E-3	7E-4	4E-4	9E-5
Optical charge generation efficiency	0.4	0.8	0.8	0.8	0.25
Langevin recombination efficiency	0.1	0.2	0.2	0.2	0.1

It is anticipated that electron mobility increases as PCBM percentage increases, while hole mobility decreases as PCBM percentage increases, which is equivalent to increase of P3HT concentrations. Since PCBM acceptor carries holes, the increasing amount of PCBM leads to an enhanced electron transport thereby improvement of the electron mobility. Similarly, the increasing amount of P3HT donor results in the hole mobility enhancement. These mobility values well match with experimental results reported in literature.^{76,77} Typically 1:1 weight ratio of P3HT and PCBM is used to obtain nanoscale interpenetrating film morphology for efficient

exciton dissociation and leads to a high optical charge generation efficiency.⁷⁸⁻⁸¹ With above consideration, the charge generation efficiencies in 40% - 60% PCBM are reasonably set to be higher than those in 20% and 80% PCBM active layer. In terms of charge generation efficiency difference between 20% PCBM layer and 80% PCBM layer, the higher concentration of P3HT, the more chance of charge generation because P3HT is the main material that absorbs sunlight and produces electron-hole pairs. Thus the charge generation efficiency in 20% PCBM (80% P3HT) is set to be a little bit higher than that in 80% PCBM active layer. It is expected that Langevin recombination efficiency has similar dependence on PCBM percentage as charge generation efficiency. According to the following equation, the Langevin recombination efficiency depends on charge carrier mobility and concentrations.¹¹⁴

$$\gamma = (\mu_n + \mu_p)np \quad (1)$$

where γ is Langevin recombination rate, μ_n and μ_p are electron mobility and hole mobility, respectively with n and p as electron and hole concentrations. Since there is no big difference in sum of electron and hole mobility ($(\mu_n + \mu_p)$) as PCBM percentage varies, the Langevin recombination efficiency is strongly depends on the generated charge carrier concentrations. Because more electrons and holes are generated in 40% PCBM, 50% PCBM and 60% PCBM active layers, a higher np value results in the higher Langevin recombination efficiency. Therefore, the Langevin recombination efficiencies at 40% - 60% PCBM levels are reasonably set to be higher than those in 20% PCBM and 80% PCBM active layers. With the listed parameter values in Table 3.1 as input, the PSC efficiency in SETFOS modeling is comparable with reported values from experiments.^{82,113} Once these electronic parameters at different PCBM percentages are validated, organic bulk heterojunction solar cells with different vertical composition profiles are investigated.

3.3 Result and Discussion

Figure 3.2(a) shows the simulated J-V characteristics of PSC with different vertical configurations. The power-conversion efficiency extracted from these J-V curves are summarized in Figure 3.2(b). Organic bulk heterojunction solar cells with uniform composition profile demonstrate the highest efficiency of 3.99%, followed by charge transport favorable structure with efficiency of 3.79%. J-V curves from these two vertical configurations show square-like shape. PSCs with sandwich II and charge transport unfavorable configurations show efficiency of 2.5% and 2.19%, respectively. The poorest device performance comes from sandwich I configuration. The lowest efficiency of 1.72% results from severe S-shape J-V curve.

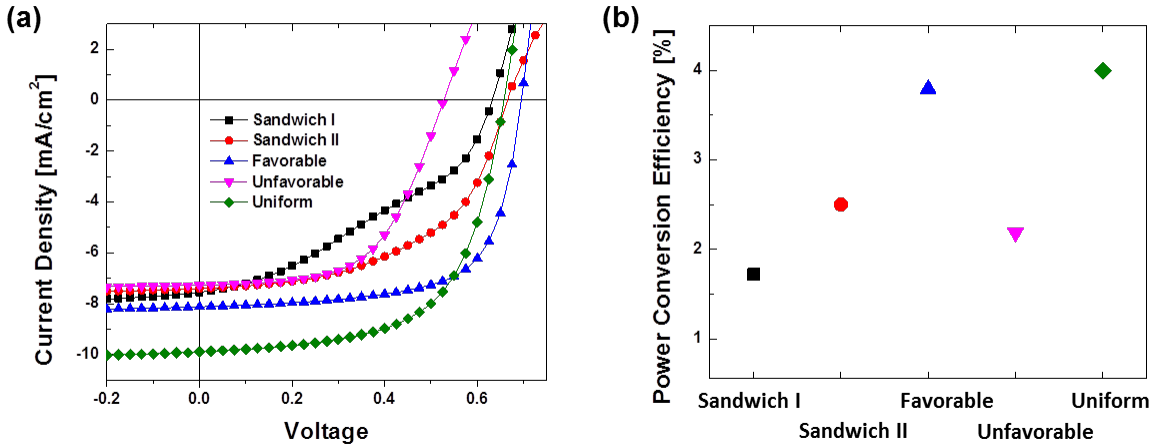


Figure 3.2. (a) J-V characteristics from SETFOS simulation, and (b) PSC efficiencies of sandwich I, sandwich II, charge transport favorable, unfavorable and uniform vertical configurations.

In order to better understand the effect of vertical configurations on the efficiency, the light absorbance from active layer, external quantum efficiency, and important output

characteristics, including open-circuit voltage (V_{oc}), short-circuit current (I_{sc}), and fill factor (FF), are examined. As shown in Figure 3.3(a), the sunlight absorption in active layer with different vertical configurations is similar. The slight difference may come from light reflection at the layer interface, which can be ignored. Figure 3.3(b) shows the external quantum efficiency (EQE), which is defined as ratio of output charge carriers to the input photons. The uniform configuration has the highest external quantum efficiency followed by charge transport favorable structure. The equal amount of mixture of P3HT donors and PCBM acceptors results in the largest interface area for efficient exciton dissociation. The charge transport favorable configuration facilitates both electron and hole transport in the active layer and charge carrier collection at the electrodes, consequently leading to less recombination and greater output carriers. The short current density shown in Figure 3.3(c) matches well with external quantum efficiency. The highest EQE from the uniform configuration has the largest current density followed by charge transport favorable structure. Figure 3(d) shows the variation of open-circuit voltage. Of all different vertical configurations, the higher values occur in charge transport favorable and uniform structures while the lowest one appears in the unfavorable configuration. Since V_{oc} is determined by the ultimate charge accumulation at electrodes, the higher the charge generation from uniform mixing and less recombination from charge transport favorable structure, the greater the charge carrier accumulation at the electrodes, leading to larger open-circuit voltage. It is anticipated that charge transport unfavorable structure has the largest charge carrier recombination, consequently resulting in the lowest V_{oc} .

Figure 3(e) exhibits the variation of the fill factor. PSCs with charge transport favorable structure show the highest fill factor followed by uniform configuration. Sandwich and charge transport unfavorable structures have relative low fill factor, particularly, the sandwich I

structure has the lowest fill factor. It is widely known that the fill factor mainly depends on charge carrier recombination, series resistance and shunt resistance. Series resistance usually comes from contact and material resistance, while shunt resistance results from current leakage, i.e. the charge carriers move to the opposite direction and are collected by the wrong electrode. Low recombination, small series resistance and large shunt resistance lead to a high fill factor. The charge transport, recombination and current leakage could be explained using energy band diagram as shown in Figure 3.4. The charge transport favorable and uniform vertical configurations facilitate electrons movement from LUMO energy level toward Al cathode and holes movement from HOMO level to ITO anode (Figure 3.4(a)), resulting in low charge carrier recombination and no leakage current, thereby high fill factor. As illustrated in Figure 3.4(b, c, d), sandwich and charge transport unfavorable structures always have energy barriers for electrons transport and collection at cathode and holes at anode, consequently leading to high recombination and low fill factor. Particularly electrons at the LUMO energy level in sandwich I structure could freely move toward both Al cathode and ITO anode. Those electrons collected at ITO anode cause leakage current, severely reducing the shunt resistance thereby the lowest fill factor.

$$PCE = \frac{V_{oc}I_{sc}FF}{P_{in}}$$

where P_{in} is input power. Based on the equation of power-conversion efficiency, PCE depends on V_{oc} , J_{sc} , and FF . The increase of any of these important parameters will improve the PCE. Uniform and charge transport favorable vertical composition profile demonstrate large values in all these three categories, leading to high PCE. In the contrast, all these three electronic properties for PSCs with charge transport unfavorable and sandwich structures fall in low values, particularly sandwich I has the smallest fill factor, resulting to the lowest PCE. It is safe to

conclude that uniform and charge transport favorable vertical composition profiles are desirable to achieve high power-conversion efficiency in organic polymeric bulk heterojunction solar cells.

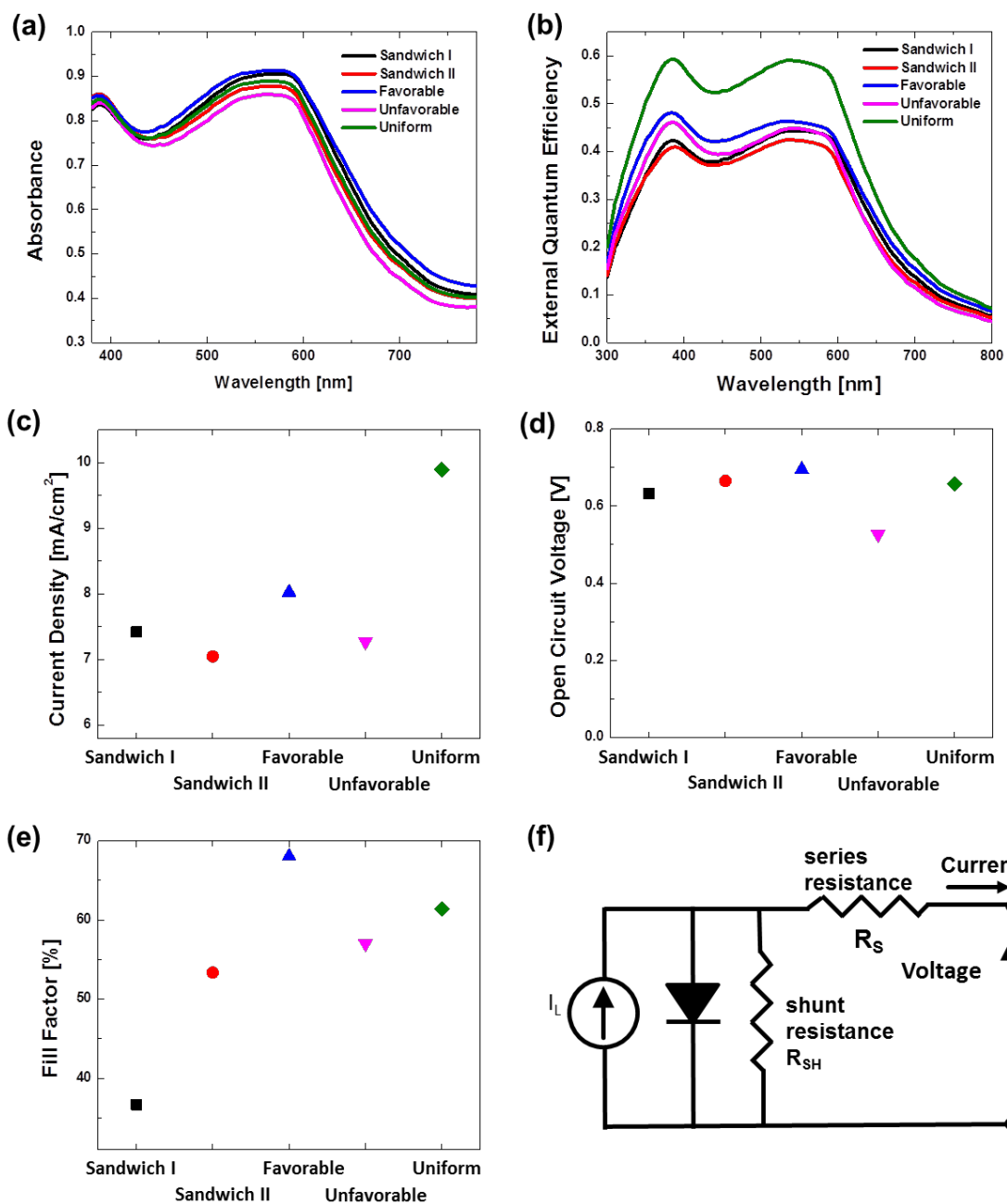


Figure 3.3. Solar cell output characteristics of (a) open circuit voltage, (b) absorbance spectrum, (c) short circuit current, (d) external quantum efficiency, (e) fill factor, and (f) equivalent circuit.

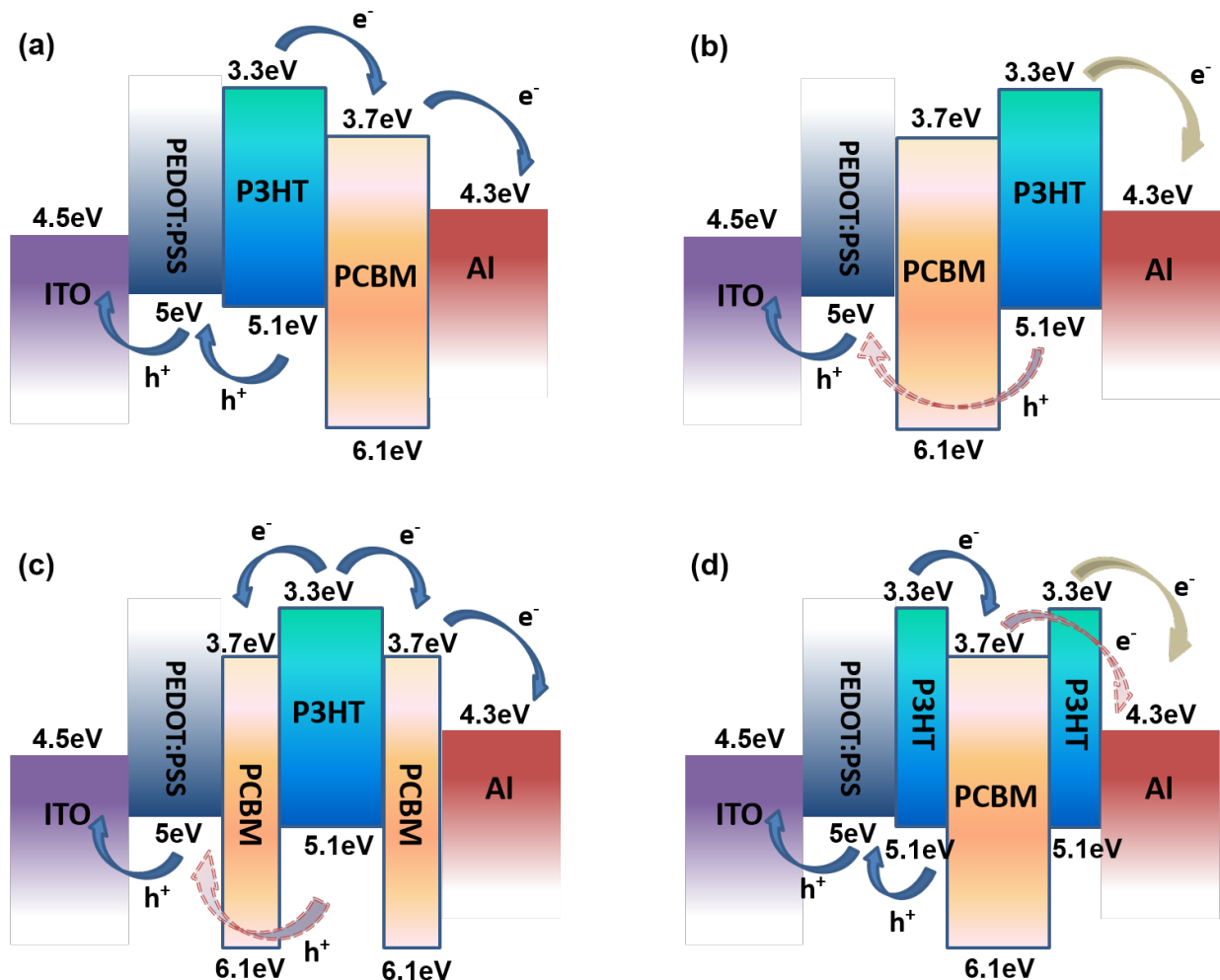


Figure 3.4. Energy band diagram of (a) sandwich I, (b) sandwich II, (c) favorable and (d) unfavorable configuration.

3.4 Vertical Configuration in Inverted Solar Cell Structure

In addition to investigate the effect of vertical composition profile in regular polymer solar cells, we also study such effect in inverted polymer solar cells. In regular organic bulk heterojunction solar cells, electrons move to the top and collected at the Al cathode, while holes move downward through PEDOT:PSS hole transport layer and are collected at ITO anode. In contrast, in inverted polymer solar cells electrons move downward through ZnO electron

transport layer and are collected at ITO cathode, while hole move upward and are collected at Ag anode. The difference between regular and inverted organic bulk heterojunction solar cell mainly lies in the opposite charge transport directions and respective collecting electrodes. Figure 3.5 shows the different vertical composition profiles in inverted solar cell structure. The charge transport favorable and unfavorable configurations are opposite to those in regular solar cell structure because of the opposite direction of electron and hole transport.

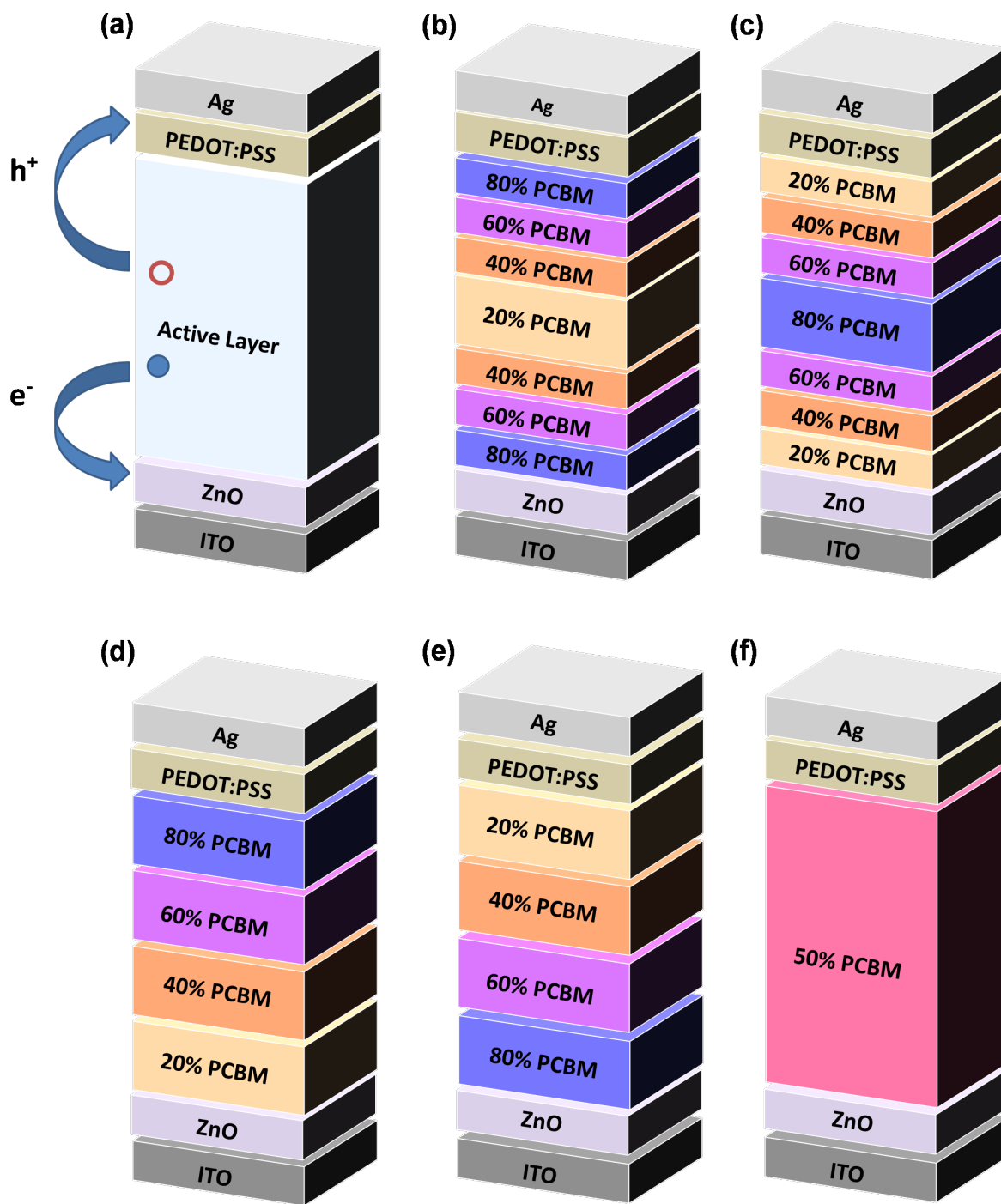


Figure 3.5. Schematic of (a) direction of electrons and holes transport in the active layer, and various vertical composition profiles (b) sandwich I, (c) sandwich II, (d) charge transport favorable, (e) unfavorable, and (f) uniform configuration of active layer in inverted PSC structure.

Figure 3.6 (a) and (b) show the simulated J-V characteristics and extracted PCE. The same as in regular polymer solar cells, the high PCE occurs for PSCs with charge transport favorable and uniform vertical composition profile, while sandwich and charge transport unfavorable configuration show low power-conversion efficiency.

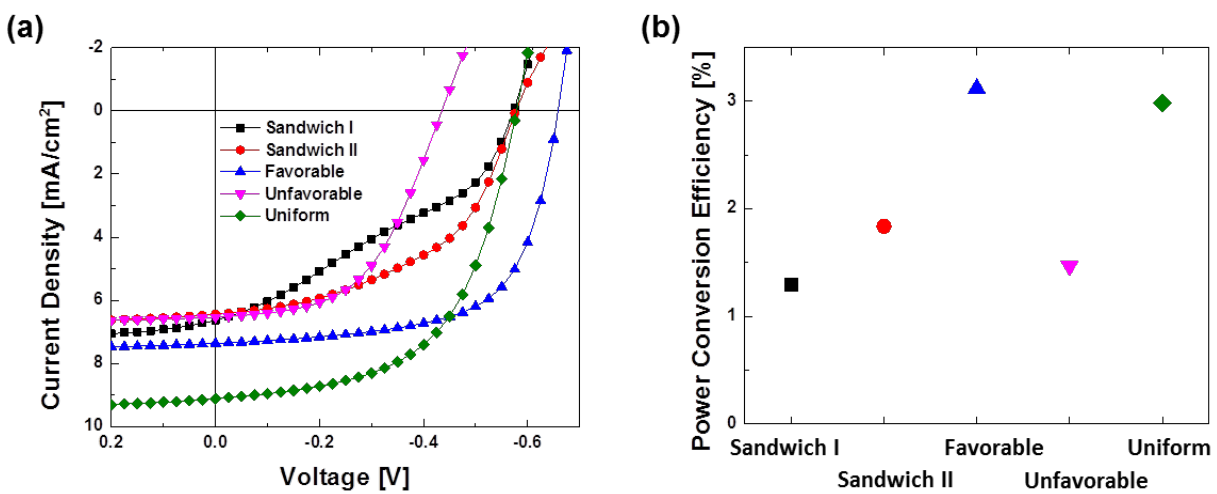


Figure 3.6. (a) J-V characteristics from SETFOS simulation, and (b) PSC efficiencies of sandwich I, sandwich II, charge transport favorable, unfavorable and uniform vertical configurations.

The same analysis as in regular structure is applied for inverted solar cells. As shown in Figure 3.7 (a), absorbance spectrums are similar among different vertical configurations. However, EQE presents a big variety as demonstrated in Figure 3.7(b). The uniform configuration still has the highest external quantum efficiency followed by charge transport favorable structure. The exciton dissociation becomes the largest when the ratio between P3HT and PCBM is 1:1. The charge transport favorable configuration facilitates both electron and hole

transport in the active layer and charge carrier collection at the electrodes. The short current density shown in Figure 3.7(c) matches well with external quantum efficiency. The highest EQE from the uniform configuration has the largest current density followed by charge transport favorable structure. Figure 3.7(d) shows the variation of open-circuit voltage. The higher values occur in uniform structures and charge transport favorable while the lowest one appears in the unfavorable configuration, which can also be explained by charge accumulation. The higher charge generation from uniform mixing and less recombination, the greater the charge carrier accumulation at the electrodes, which leads to larger open-circuit voltage. Largest charge carrier recombination in charge transport unfavorable structure results in the lowest Voc. Figure 3.7(e) exhibits the variation of the fill factor. PSCs with charge transport favorable structure show the highest fill factor followed by uniform configuration. Sandwich and charge transport unfavorable structures have relative low fill factor, particularly, the sandwich I structure has the lowest fill factor.

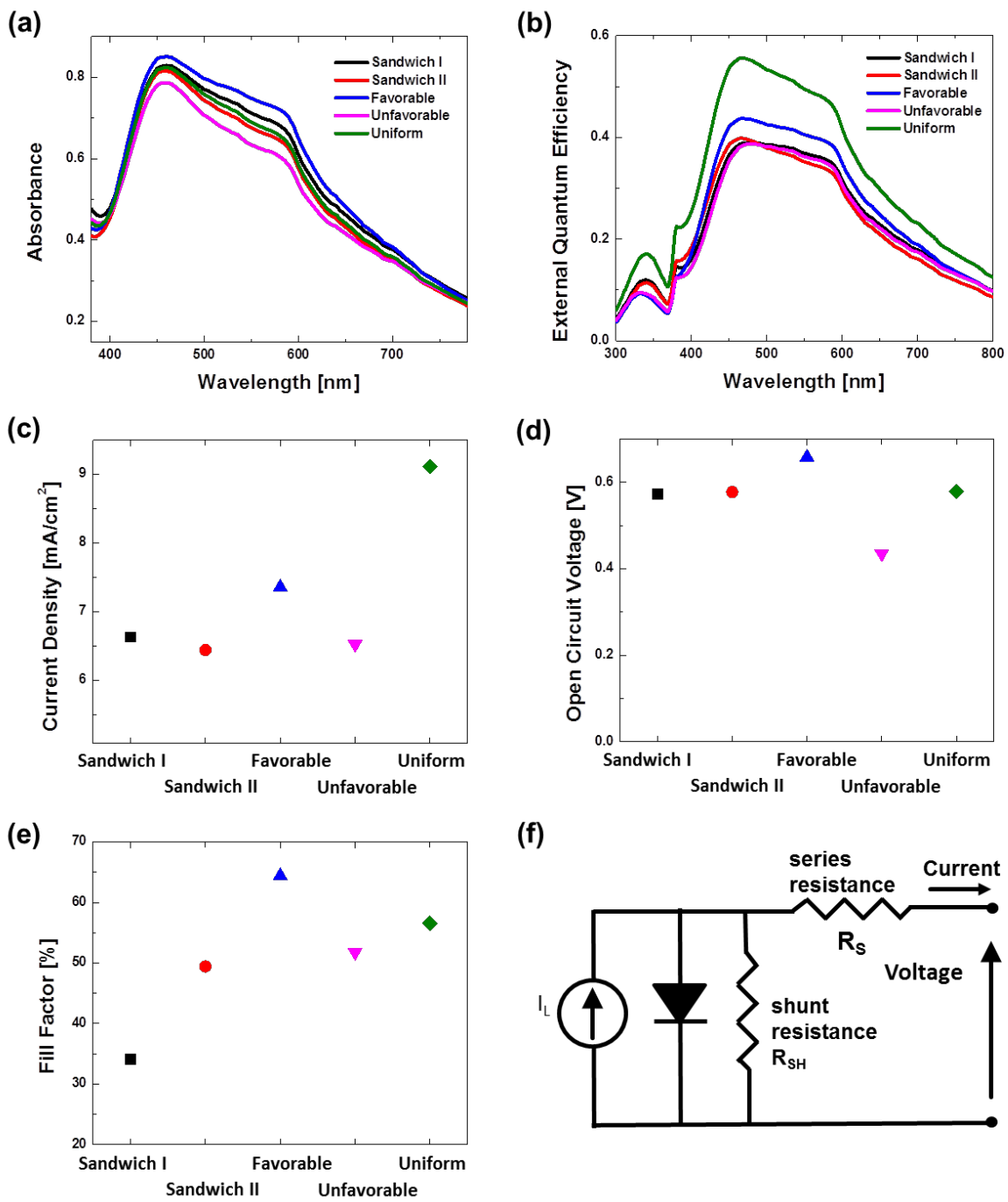


Figure 3.7. Solar cell output characteristics of (a) absorbance spectrum, (b) external quantum efficiency, (c) short circuit current, (d) open circuit voltage, (e) fill factor, and (f) equivalent circuit.

The charge transport, recombination and current leakage could be explained using energy band diagram as shown in Figure 8. The charge transport favorable and uniform vertical configurations facilitate electrons movement from LUMO level of P3HT/PCBM toward Ag cathode and holes movement from HOMO level to ITO anode (Figure 3.8(a)), resulting in low charge carrier recombination and no leakage current, thereby high fill factor. As illustrated in Figure 3.8(b, c, d), sandwich and charge transport unfavorable structures always have energy barriers for electrons transport and collection at cathode and holes at anode, consequently leading to high recombination and low fill factor. Particularly electrons at the LUMO energy level in sandwich I structure could freely move toward both Ag cathode and ITO anode. Those electrons collected at ITO anode cause leakage current, severely reducing the shunt resistance thereby the lowest fill factor. The same as for regular solar cells, it is still safe to conclude that uniform and charge transport favorable vertical composition profiles are also desirable to achieve high power-conversion efficiency in organic polymeric bulk heterojunction solar cells with inverted structure.

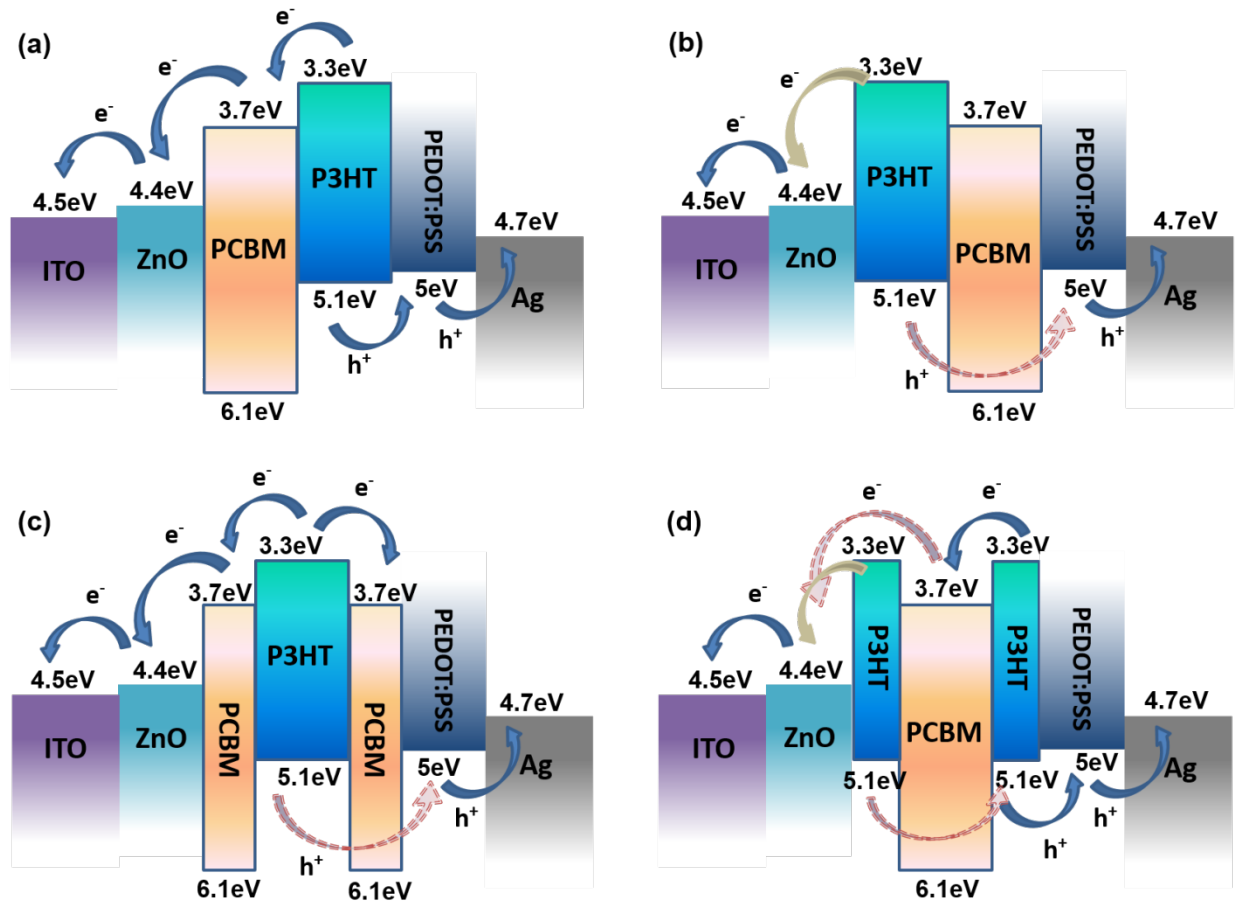


Figure 3.8. Energy band diagram of (a) favorable, (b) unfavorable, (c) sandwich I and (d) sandwich II configuration.

3.5 Summary and Conclusion

Vertical configuration of polymer solar cells is chosen as a valuable topic for several reasons. (1) Polymer solar cell has bottom-up structure. Charge carriers are transported in vertical direction. The quality of “pathway” directly determines the performance of solar cell devices. (2) The distribution of donor and acceptor not only has an impact on charge carrier separation but also influence their transportation. Normally, electrons and holes are generated in donor material and separated at the interface of donor and acceptor. Proper number of acceptor

molecules around donor results in the best charge carrier separation. As an ideal case, uniform distribution of donor and acceptor results in the most efficient exciton separation due to the largest interfaces of donor and acceptor. On the other hand, smooth charge carrier transportation requires an increasing amount of donor/acceptor to assist hole/electron to reach anode/cathode, as in the favorable vertical configuration. Charge transport favorable vertical configuration enlarges the mean free path and causes less recombination before charge carriers reach electrodes.

To conclude, different vertical composition profiles have been modeled for both regular and inverted organic solar cells. The results show a remarkable effect from vertical configuration on device performance. In both regular and inverted structures, Favorable and Uniform configurations always give the highest efficiency, while Sandwich and Unfavorable configurations tend to have poor performance. In addition, the simulation study also provides an in-depth understanding of physical mechanisms behind the different vertical configurations of active layer and the effect on solar cell performance.

CHAPTER 4

ZINC OXIDE FILM PREPARED BY DIFFERENT METHODS FOR ELECTRON TRANSPORT LAYER IN ORGANIC SOLAR CELLS

4.1 introduction

Zinc oxide (ZnO) has attracted a great deal of interest due to its electronic properties. As a semiconductor with a wide bandgap (3.4eV), ZnO has been applied in a various areas, such as image sensor, optoelectronics.⁸⁰⁻⁸³ Also ZnO nanostructures have been used for fabrication of a wide variety of devices including light emitting diodes, laser diodes and field emission devices, piezoelectric devices, photovoltaic devices, catalysis, hybrid solar cells and gas sensors.⁸⁴⁻⁸⁹ The high electron mobility of ZnO makes it a favorable choice for serving as an electron transport layer in organic polymer solar cells with inverted structure. In the inverted solar cells, ZnO is deposited on top of ITO glass to assist electrons transporting to cathode. Combined ZnO with top electrode, which is Ag or Au, researchers managed to improve the stability of organic solar cell.⁹⁰⁻⁹² There are various ways to fabricate a ZnO electron transport layer. Steven and his colleagues successfully used ZnO nanoparticles as electron selective layer which prevents from high temperature and vacuum requirement used in traditional ZnO preparation method.⁹⁰ Kwong and his research group demonstrated sol-gel method to deposit ZnO layer.⁹¹ Although various methods can be used to make ZnO films, the quality of these films could be different, which

would influence the performance of inverted polymer solar cells. To our best knowledge, no group ever focused on the quality of ZnO films on with diverse ways of fabrication and their effect on solar cell efficiency.

In this project, four different ZnO films are prepared to serve as electron selective layer in P3HT-PCBM based solar cells, including two kinds of ZnO films and two ZnO nanorods, as shown in Figure 4.1. ZnO films made of atomic layer deposition (ALD) and sol-gel methods were used to fabricate a device as shown in Figure 4.1(a). In order to increase the interface between ZnO and P3HT-PCBM active layer, ZnO nanorods are grown from seed layer made of ALD and sol-gel methods, as shown in Figure 4.1(b). Surface morphology and quality of films from different methods were characterized by scanning electron microscopy (SEM) and atomic force microscopy (AFM). Finally, inverted organic solar cells were fabricated with difference ZnO films as electron transport layer and their performances are compared.

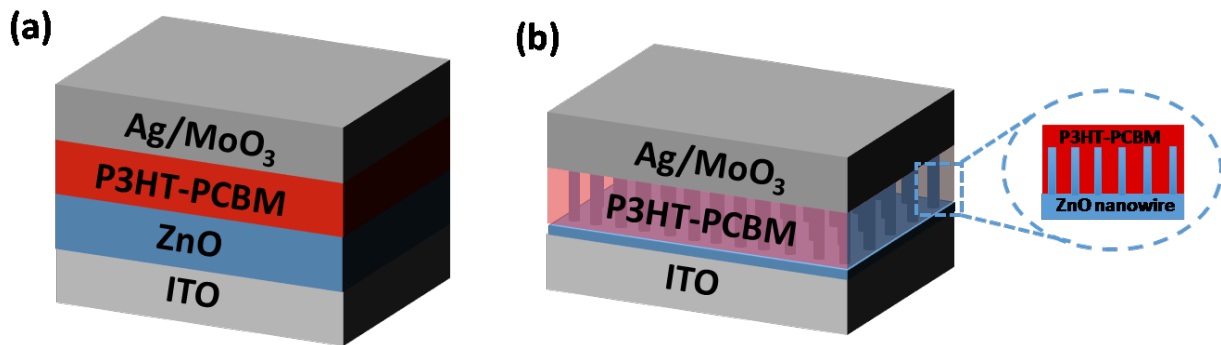


Figure 4.1 Schematic of (a) ZnO film, and (b) ZnO nanorods in P3HT-PCBM based inverted solar cells.

4.2 Experimental

P3HT polymer was purchased from Aldrich and used as received. ITO glass substrates were first cleaned by detergent, DI water, acetone and IPA consequently for each of 30 minutes. Then substrates were treated by oxygen plasma for 1 minute at the power of 30W. After substrate cleaning, ZnO film from various preparation methods is deposited on the ITO substrate. P3HT-PCBM blending solution was spin-coated on the top of ZnO electron transport layer at the speed of 900rpm for 45s followed by annealing at 140°C for 15 minutes. After deposition of active layer, hole transport layer MoO₃ and anode metal silver were thermally evaporated at the rate of 0.2 and 0.5 Å/s, to form 8nm MoO₃ and 50nm Ag film, respectively.

As mentioned above, in this study ZnO films will be prepared using different techniques, including sol-gel method and ALD deposition. The solution in sol-gel method was prepared using zinc acetate dehydrate [Zn(CH₃COO)₂·2H₂O] as a precursor, IPA [C₃H₇OH] as a solvent and monoethanolamine as a stabilizer. The molarity (M) was fixed at 0.1 M. After heated up at 60°C for 24 hours with stirring, the solution was filtered through a filter (0.2 μm) to removed undissolved particles. The solution was then spin-coated on pre-treated substrates followed by annealing at 200°C for an hour to form a 60nm ZnO film. With ALD technique, ZnO film was created by using diethylzinc and oxygen as two precursors to fabricate 60nm film followed by annealing at 200°C for an hour.

ZnO films with nanorods topography were created using hydrothermal method with seed layer deposited by ALD and sol-gel method, respectively. The same sol-gel method with a concentration of 0.05 M was used to deposit 20nm ZnO seeded layer. Meanwhile 20nm seed layer was also prepared from ALD deposition. Finally, the substrates with thin seed layers were

immersed in $\text{Zn}(\text{NO}_3)_2$ and HTMA blend solution (1:1 volume) and put it in oven at 90°C for 1 hour to grow nanorods of 60nm.

4.3 Results and Discussion

The fabricated organic solar cells with different kinds of ZnO films as electron transport layer were characterized and typical I-V curves were shown in Figure 4.2. ZnO film based solar cells always have larger open circuit voltage (V_{oc}), short circuit current (I_{sc}) and fill factor (FF) than those from ZnO nanorods. Especially, solar cells with ZnO film from sol-gel method give a square-like curve with highest V_{OC} and I_{SC} . The inverted solar cells from ALD film show a S-shape I-V curve, which indicates poor film quality and large series resistance. For ZnO nanorods based on solar cells, the devices from ALD seeded nanorods show slightly higher V_{oc} but lower I_{sc} compared to those from sol-gel seeded nanorods. Overall, inverted solar cells based on ZnO film have better performance than those using ZnO nanorods as electron transport layer. Quantity data for device performance are listed in Table 1.

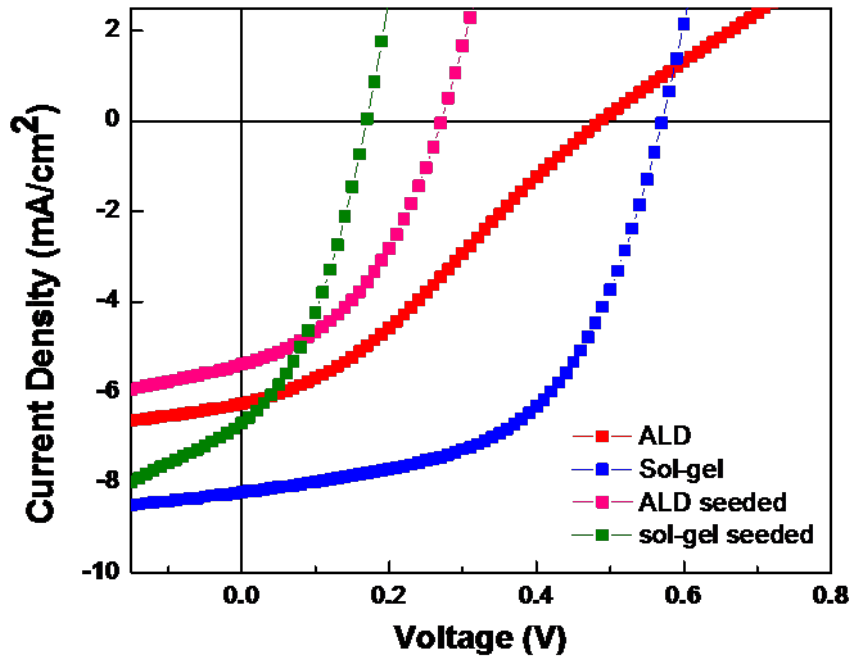


Figure 4.2 Comparison of I-V curves for inverted solar cells with ZnO from ALD, sol-gel method, ALD seeded nanorods and sol-gel seeded nanorods.

Table 4.1. Solar cell performance with different kinds of ZnO deposition methods.

	Voc	Isc	FF	PCE
ALD film	0.49	6.239	31.13	0.95
Sol-gel film	0.57	8.221	53.94	2.53
ALD seeded nanorods	0.27	5.398	41.64	0.61
Sol-gel seeded nanorods	0.24	4.558	31.14	0.34

Surface topography of ZnO nanorods grown from sol-gel seeded film and ALD seeded layer was characterized by SEM, as shown in Figure 4.3(a) and (b), respectively. Both images share the same scale bar. The nanorods grown from ALD seeds look denser than that from sol-gel seeds. More denser ZnO nanorods are anticipated to efficiently block hole transport, resulting in higher higher Voc and lower Isc as shown from I-V characteristics in Figure 4.2. The morphologies of sol-gel grown films and ALD deposited films were scanned by atomic force

microscopy (AFM), as shown in Figure 4.3(c) and (d), respectively. The roughness from sol-gel grown films is about 0.425nm, while that from ALD is about 3.486nm. Several reasons are expected to cause low device performance with ZnO nanorods compared to that from ZnO film. Usually, the more smooth the active layer in organic solar cells, the better contact between active layer and surrounding films, resulting in better performance. ZnO films have definitely more smooth and uniform surface than nanorods, which reduce contact resistance, leading to higher V_{oc} and I_{sc} . Comparing solar cell performance between sol-gel grown ZnO films and ALD deposited films, the devices based on sol-gel grown ZnO films have better performance than those from ALD deposited films due to low active layer surface roughness. Although nanorods are able to increase surface area of ZnO electron transport layer, they could also introduce surface defects and increase resistance for charge transport through nanorods, which could reduce the solar cell performance.

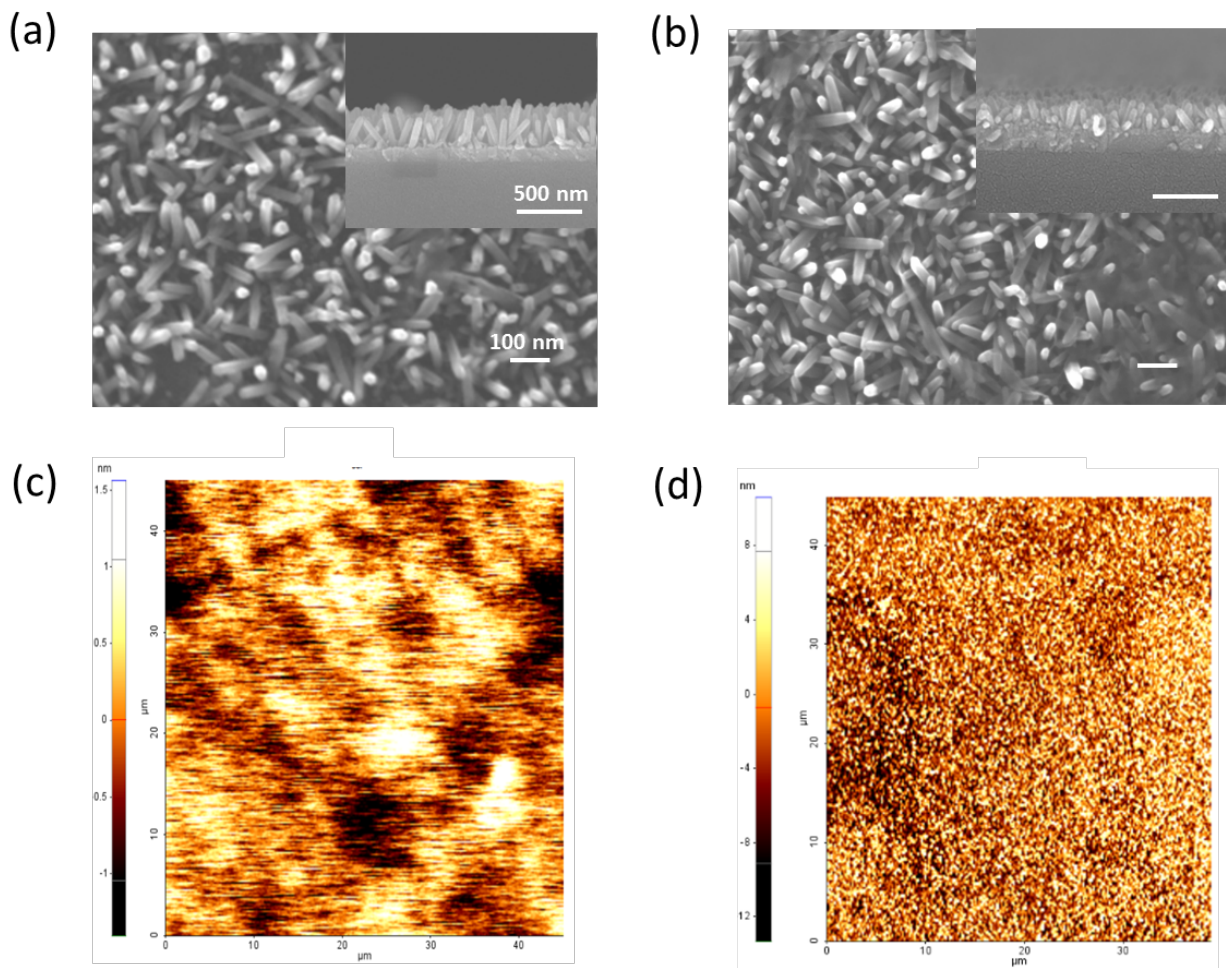


Figure 4.3 SEM image of ZnO nanorods from (a) sol-gel seeded method and (b) ALD seeded method. Inset monograph is the side-view of nanorods. AFM image of (c) sol-gel film and (d) ALD deposited film.

4.4 Conclusion

In this project, ZnO films and ZnO nanorods are deposited and grown using two different methods, ALD and sol-gel method. The performance of organic solar cells using these ZnO layers as electron transport layer is compared. Devices based on ZnO films demonstrated higher efficiency than those from ZnO nanorods. Although nanorod morphology increases the interface between ZnO and active layer, the surface roughness, possible surface defects and increased

charge transport resistance through nanorodes cause overall series resistance increase, resulting in a poor performance and low efficiency. Compare ZnO films prepared by ALD deposition and sol-gel growth, solar cells with ZnO film made by sol-gel method show better performance (higher Voc, Isc and fill factor) thereby a higher efficiency due to lower surface roughness.

CHAPTER 5

ORGANIC POLYMER SOLAR CELLS FABRICATION BY MULTI-LAYER INKING AND STAMPING

5.1 introduction

Renewable and low-cost energy sources have gained increased attention as the global supply of fossil fuels decreases and the modern energy crisis intensifies. Since the annual solar radiation from the sun produces significantly more energy than that consumed by the entire world's population in a year, much research have been invested into photovoltaic cells to harvest the sun light energy.^{57, 58, 63, 93-95} Although current solar energy produced by traditional inorganic solar cells seems like a promising solution, these cells are ultimately too expensive to be mass-produced. In contrast, organic polymer solar cells (PSCs) serve as a more viable possibility in the future in both cost and energy efficient to replace conventional energy sources.⁹⁶⁻⁹⁸ Instead of using the silicon wafer-based processing predominantly found in inorganic solar cells, most PSCs use less expensive low-temperature solution processing methods, such as spin-coating on ITO glass substrates. However, such spin-coated PSCs have certain limitations on solar cell versatility. Primarily, spin-coated cells are both difficult and relatively expensive to fabricate over a large area. Furthermore, thin films are unable to be spin-coated with the same uniformity on flexible substrates as on rigid ITO glass substrates. Therefore, spin-coated PSCs are

incompatible with the high throughput process of roll-to-roll printing required for efficiently mass-production of solar cells.

Recently some inexpensive high yield pattern transfer techniques have been developed to overcome the incompatibility of certain organic electronics with flexible substrates and roll-to-roll printing.⁹⁹⁻¹⁰⁴ For example, the inking and stamping pattern transfer method, which uses cost-efficient PDMS elastomeric stamps, has been applied to successfully transfer conducting polymer poly(3,4-ethylenedioxythiophene) (PEDOT:PSS) to make organic thin film transistors (OTFTs). Multi-layer inking and stamping of metals and polymers in a single step has also been developed to fabricate polymer light-emitting diodes (PLEDs) on both ITO and flexible substrates. Direct multilayer pattern transfer is able to preserve the functionality of the patterned polymer layers in organic devices and still maintain high-resolution transferred patterns.^{105, 106} Yet, in spite of the success in producing PLEDs and OTFTs using the inking and stamping technique, the same procedure has not been applied to PSC fabrication.

In this study, an improved multi-layer inking and stamping technique was developed to successfully fabricate PSCs on both ITO glass and PET flexible substrates, and a reliable experimental procedure for uniform metal deposition and a minimum of additives were established to produce both a high yield pattern transfer and maximum solar cell efficiency. With the fabricated PSCs from the multi-layer inking and stamping technique, the effects of the additives on the pattern transfer and overall performance of polymer solar cells were systematically investigated.

5.2 Experimental

P3HT and PCBM were purchased from Solarmer and Nano-C respectively and used as received. The chemical structures of P3HT and PCBM were shown in Figures 5.1(a) and (b), respectively. ITO glass was cleaned in detergent, DI water, acetone and IPA in sequence, and treated with oxygen plasma at 30W for 5 minutes to increase the ITO's surface energy for wetting. A silicon master mold, which was previously fabricated by photolithography and reactive ion etching (RIE), was put into a petri dish with pattern-side up. Sylgard 184 silicone elastomeric base mixed with curing agent at a weight ratio of 8:1 was poured into the petri dish to duplicate the patterns. Then the whole petri dish was put in a vacuum oven overnight at room temperature to remove excess bubbles in the PDMS solution. After thermal curing at 100°C for 1.5 hours, the PDMS solution was completely solidified. Finally PDMS stamps were made with duplicated patterns when peeling off from the silicon master mold.

In making polymer solar cells using multi-layer inking and stamping, the PDMS stamp was first attached to the sample holder for metal Al deposition. Instead of directly putting the PDMS stamp on the metal holder, a glass substrate was placed in between to thermally isolate the stamps from heated metal holder, which reduces possibility for generating cracks during metal deposition. 30 nm of gold were sputtered onto the PDMS stamp followed by 50 nm of aluminum deposited by thermal evaporation at a rate of 2Å/s. P3HT and PCBM at 1:1 weight ration and concentration of 25mg/ml in chlorobenzene was spin-coated onto the PDMS at a spin-speed of 900 rpm for 45s. The PDMS was then treated with oxygen plasma at 30W for 10 seconds followed by spin-coating PEDOT:PSS onto the PDMS at 5000 rpm. The plasma treatment increases surface energy for uniform coating of hole transport PEDOT:PSS layer. In order to increase the adhesive properties of the PEDOT:PSS solution on ITO substrate, various

amounts (2.5 μ l, 5 μ l, 10 μ l, 20 μ l) of 3-Glycidyoxypropyl trimethoxysilane (GLYMO) were added to 1ml of PEDOT:PSS solution and left at room temperature overnight. The chemical structure of GLYMO is shown in Figure 5.1(c). After the multi-layer inking on the PDMS stamp, the “inked” PDMS stamp is immediately stamped onto the pre-cleaned ITO substrate and placed the whole assembly on a hot plate at 80°C for 2 minutes.¹⁰⁷ The hot plate baking reduces the adhesion between PDMS and metal cathode, facilitating multilayer pattern transfer. After peeling off the PDMS stamp from ITO glass, multilayer organic solar cells are fabricated. The entire process is shown in Figure 5.2.

A current-voltage (I-V) characterization of polymer photovoltaic cells was conducted using a computer-controlled measurement unit from Agilent technologies B1500A semiconductor parameter analyzer under ambient condition with illumination of AM1.5G, 100mW/cm². Optical images, SEM and AFM are used to characterize the surface morphology of transferred patterns.

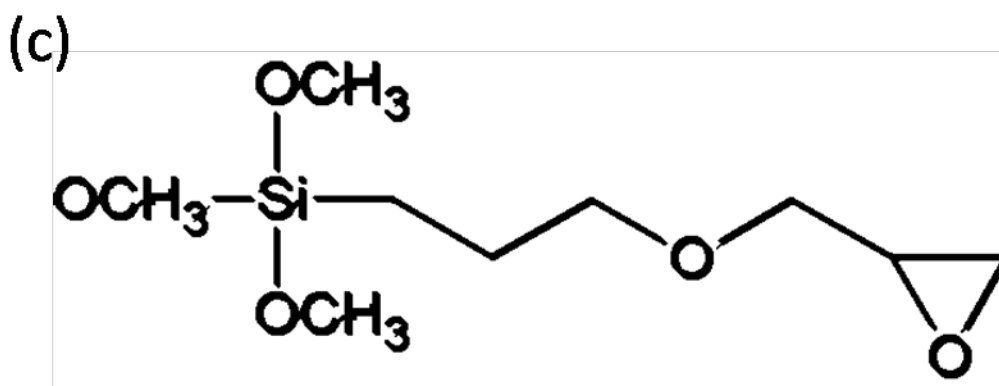
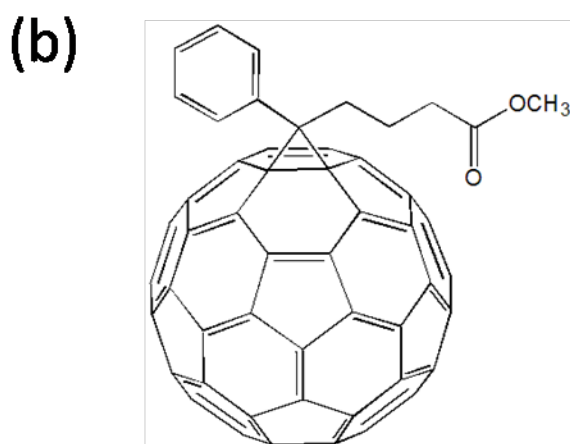
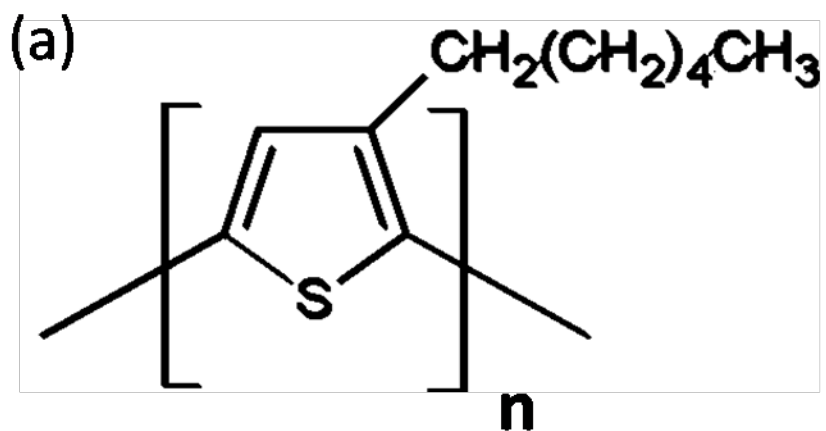


Figure 5.1. Chemical structures of (a) P3HT, (b) PCBM, (c) 3-Glycidyloxypropyl trimethoxysilane (GLYMO).

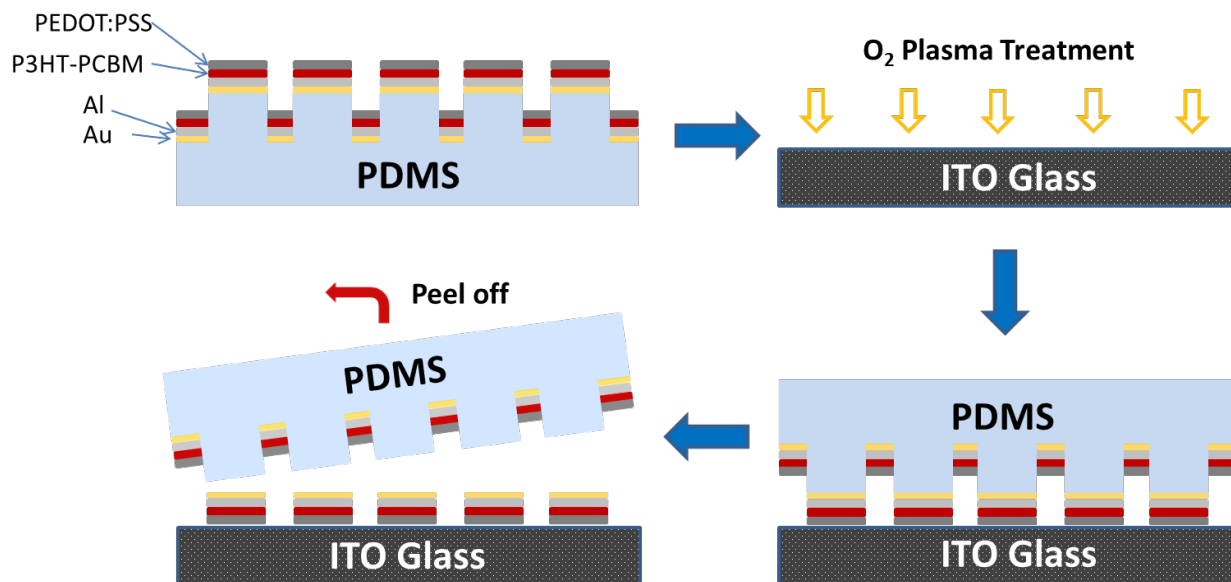


Figure 5.2. Schematic of the multilayer inking and stamping technique. Multilayer inking onto PDMS stamp following by stamping on plasma treated ITO glass. Multilayer organic solar cells are fabricated after peeling off the PDMS stamp from ITO glass.

5.3 Results and Discussion

SEM monograph of Figure 5.3(a) clearly demonstrates that high yield multi-layer pattern transfer was successfully performed to make organic polymer solar cells. Each rectangular pattern represents a separate PSC device. The relatively smooth surface and high yield of the transferred patterns with minimal deformities, such as cracks or buckles, signify an optimal metal deposition, a sufficient addition of GLYMO to the PEDOT:PSS solution, and careful handling of the PDMS stamp during the thermal evaporation and spin-coating process. The occasional small “dots” presented in the image may be due to interference of dust particles in the lab during spin-coating.

From AFM image shown in Figure 5.3(b), a clear recession can be observed, indicating good separation between transferred patterns due to optimal pressure applied during the stamping process.¹⁰⁵ The dark orange middle section with well-defined top and bottom edges represents a clear gap between two transferred patterns. The pattern separation indicates that only desired protrusion parts of materials on the PDMS stamp were transferred because of the maximum stress at the corners of the patterns. Well separated solar cell patterns allow a more accurate area measurement for each PSC device.

A clear definition of each layer rather than mixing is the key to ensure charge transport and collection at cathode and anode, respectively. In order to reveal the layer definition of metal (Au/Al), P3HT/PCBM and PEDOT:PSS thin-films on ITO glass after pattern transfer, a cross-section SEM image was taken as shown in Figure 5.3(c), in which distinctively separated edges with sharp contrast can be observed, especially between P3HT/PCBM and PEDOT:PSS layers. The well separation of these organic layers is mainly due to the facts that P3HT/PCBM dissolves in an organic solvent while PEDOT:PSS is in aqueous solution.

In addition to ITO glass substrates, successful pattern transfer was also performed on PET flexible substrates as shown in Figure 5.3(d). Note that bending the substrate with metal tweezers does not influence the morphology of the transferred patterns. This achievement demonstrates great promise for using the multi-layer inking and stamping technique to fabricate large amounts of PSC through roll-to-roll printing.

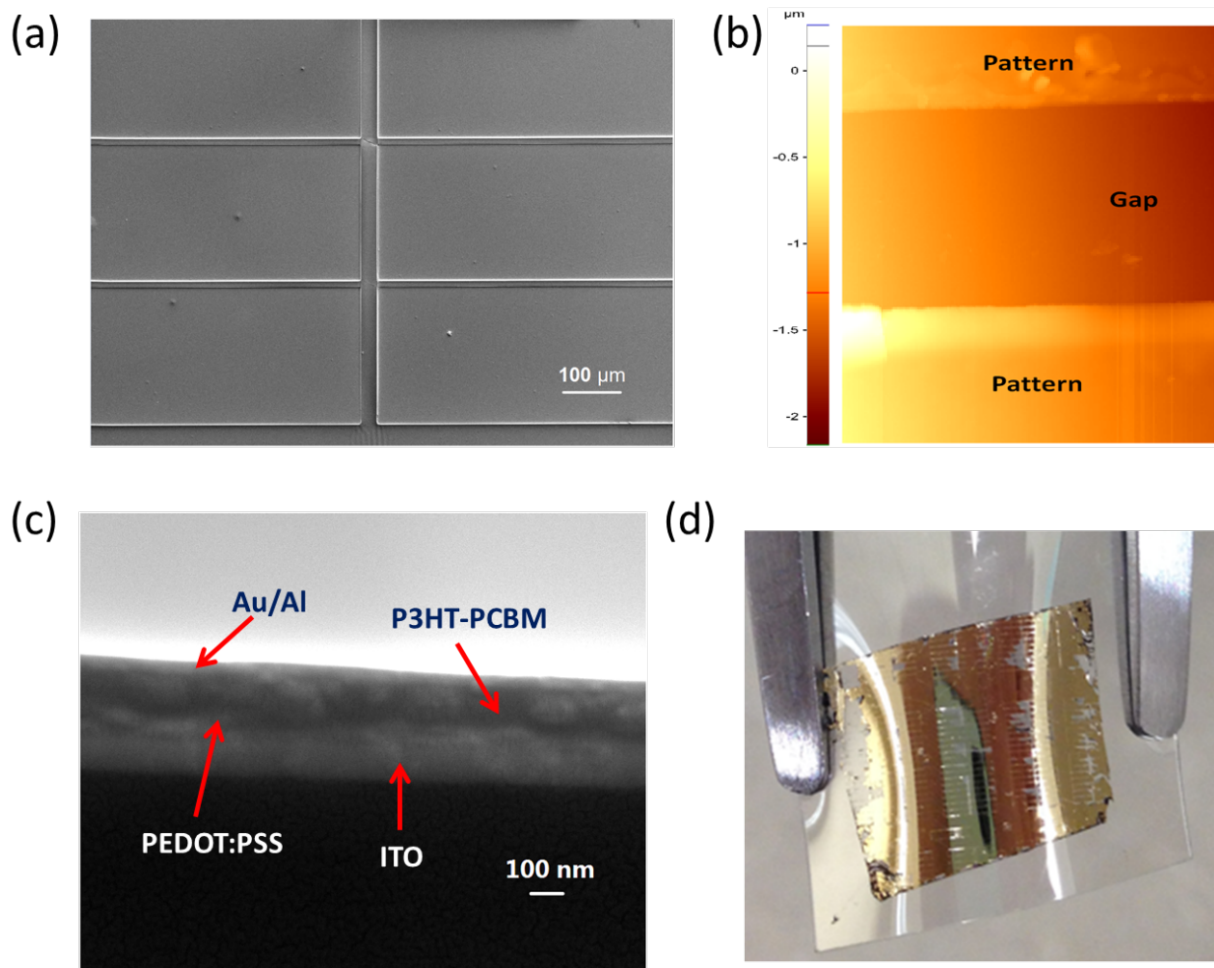


Figure 5.3. (a) SEM monograph of a high yield pattern transfer onto ITO glass substrate. (b) AFM image of the recession between two separated patterns after the pattern transfer process. (c) SEM cross-sectional image of the transferred multi-layers, Au/Al, P3HT/PCBM, PEDOT:PSS, from top to bottom on ITO glass. (d) Optical photograph of multi-layer PSCs successfully transferred onto a PET flexible substrate.

To achieve good metal contact as cathode and clear transferred patterns, a uniform metal deposition free of cracks and buckles is the first and foremost step to a high yield pattern transfer and, ultimately, to a working solar cell. Both thermal evaporation and sputtering techniques were used to deposit metal onto the patterned PDMS stamps. Only using thermal evaporation resulted in many cracks and buckles on the metal film, hindering the pattern transfer process. However, these surface deformities diminished when sputtering was used to deposit the first layer of gold

before using thermal evaporation to deposit aluminum. Since sputtering uses less heat than thermal evaporation, there is less expansion and contraction of the PDMS stamps during heating and cooling processes;¹⁰⁸ thus, the application of sputtering is able to produce a uniform metallic surface as well as influence a uniform deposition by thermal evaporation.^{109, 110} A 30 nm of gold layer by sputtering is found to result in the most uniform metal thin films. When depositing Al as the second layer using thermal evaporation, the setting of several parameters can be modulated to further improve deposition uniformity. Primarily, the deposition rate from 1Å/s to 2Å/s caused quicker crystallization of the metal layers, thus, preventing interdiffusion and resulting in distinct and uniform layers of aluminum and gold.^{111, 112} Moreover, the reduction of aluminum thickness from 80nm to 50nm was noted to reduce the amount of cracks and buckles from the thermal evaporation. Lastly, using glass backplanes as thermal isolation layer between the PDMS and the thermal evaporation sample holder had shown to further reduce surface deformities and to protect the PDMS from unintentional human mishandlings.

In addition to a uniform metal deposition, a high yield multi-layer pattern transfer also depends on the relative adhesion strengths among layers of thin-film, the PDMS stamp, and the substrate. In order for an entire stack of thin-films to be transferred, the adhesion between the PEDOT:PSS and the ITO must be the strongest of all interlayer attractions and the adhesion between the PDMS and metal must be the weakest. The addition of GLYMO into PEDOT:PSS significantly increases the adhesion of the PEDOT:PSS to the ITO substrate by preventing the PEDOT:PSS from drying out during the spin-coating process. Similarly, a thin layer of gold should be deposited first onto the PDMS stamp before depositing aluminum because the attraction of gold to PDMS is considerably less than that of aluminum. After optimization, we

identified that at least 5.0 μ L of GLYMO per 1ml of PEDOT:PSS and 30nm of gold are necessary to perform a high yield multi-layer pattern transfer.

In order to test the effect of GLYMO on PSC efficiency, a set of control experiments were performed on spin-coated solar cells with different amounts of GLYMO (0.0 μ l, 2.5 μ l, 5.0 μ l, 10.0 μ l,20.0 μ l) added into 1ml of PEDOT:PSS . Current-voltage characteristics are displayed in Figures 5.4(a) and extracted performance parameters are listed in Table 5.1. When the amount of GLYMO increases from 2.5 μ l to 5 μ l, the open circuit voltage (V_{oc}) remained relatively constant, while its short circuit current (J_{sc}) greatly increases from 4.9 mA/cm² to 6.5mA/cm², as demonstrated in Figure 5.4(a), and the fill factor (FF) increases from 36.4% to 44.6% as shown in Table 5.1, which indicates that the HOMO (highest occupied molecular orbit) and LUMO (lowest unoccupied molecular orbit) remained the same, while the series resistance inside the devices has been reduced. The reduction of series resistance could come from improved contact between PEDOT:PSS and ITO surfaces after addition of GLYMO. However, when the GLYMO concentration is further increased, the short circuit current dramatically decreases. For example, when 20 μ l of GLYMO was added, the PSC short circuit current had decreased to a value of less than 0.4%, as illustrated in Figure 5.4(b). Interestingly, we also found that no addition of GLYMO did not produce the best results. Thus, we came to the conclusion that while higher concentrations of GLYMO may significantly reduce PSC efficiency, particularly on the short-circuit current, a certain amount of GLYMO is necessary for optimal PSC performance. Based on these results seen in Table 5.1, it is concluded that 5.0 μ l of GLYMO is the ideal amount required per 1ml of PEDOT:PSS to achieve both the highest PSC efficiency and a high yield pattern transfer.

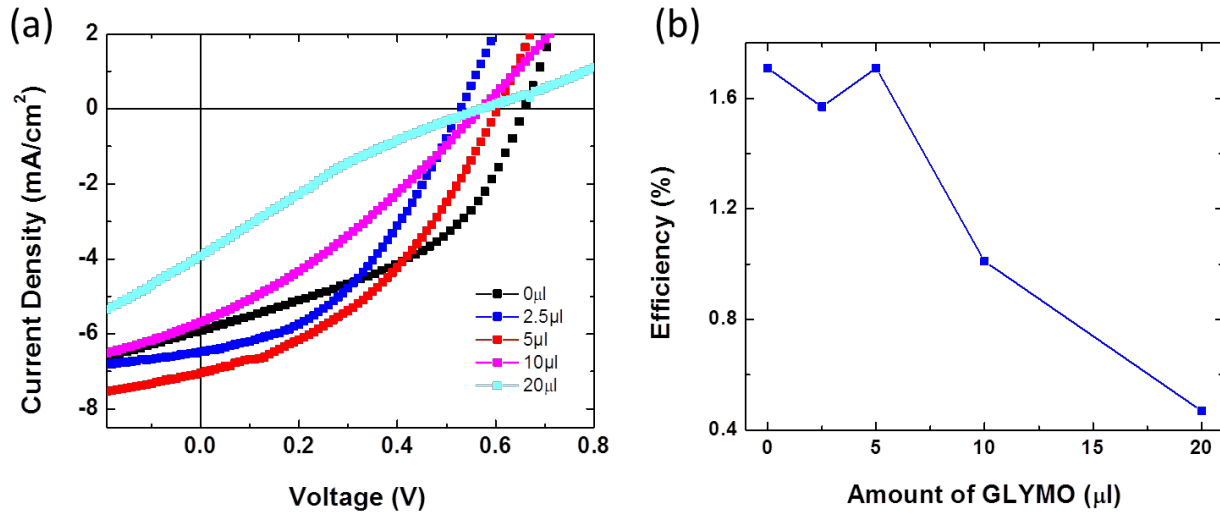


Figure 5.4. (a) I-V characterizations of spin-coated P3HT/PCBM solar cells with 0.0 μ l, 2.5 μ l, 5.0 μ l, 10.0 μ l and 20.0 μ l of GLYMO added into 1ml of PEDOT:PSS solution. (b) Comparison of PSC efficiency vs. the amount of GLYMO added into 1ml of PEDOT:PSS solution.

Table 5.1. Voc (V), Jsc (mA/cm²), FF(%), and efficiency values of spin-coated solar cells with various amounts of GLYMO added into 1ml of PEDOT:PSS solution.

	Voc (V)	Jsc (mA/cm ²)	FF (%)	Efficiency (%)
0.0ul	0.66	5.93	43.67	1.71
2.5ul	0.60	6.84	38.58	1.57
5.0ul	0.61	7.03	40.24	1.71
10.0ul	0.58	5.69	30.95	1.01
20.0ul	0.58	3.92	20.73	0.47

Finally, current-voltage measurement was performed on a pattern transferred device with 460 μ m x 1000 μ m dimensions, a 5.0 μ l:1ml GLYMO to PEDOT:PSS ratio, as shown in Figure 5.5. A Voc of 0.57V, a Jsc of 1.7 μ A/cm², FF of 21.4% and an efficiency of 2x10⁻⁴% were obtained. The Voc seems comparable to that of a spin-coated solar cells, but the Jsc is rather low.

The comparable V_{oc} indicates a good pattern transfer and a functional light absorption layer. The low current is likely caused by the oxidation of Al at the interface between Al and P3HT/PCBM, which may have led to significant degradation of the PSC device. Another effect might come from the oxygen plasma treatment on P3HT/PCBM layer since oxygen react with P3HT molecules which will change its conjugated property, resulting in difficulty of charge carrier generation and transport.

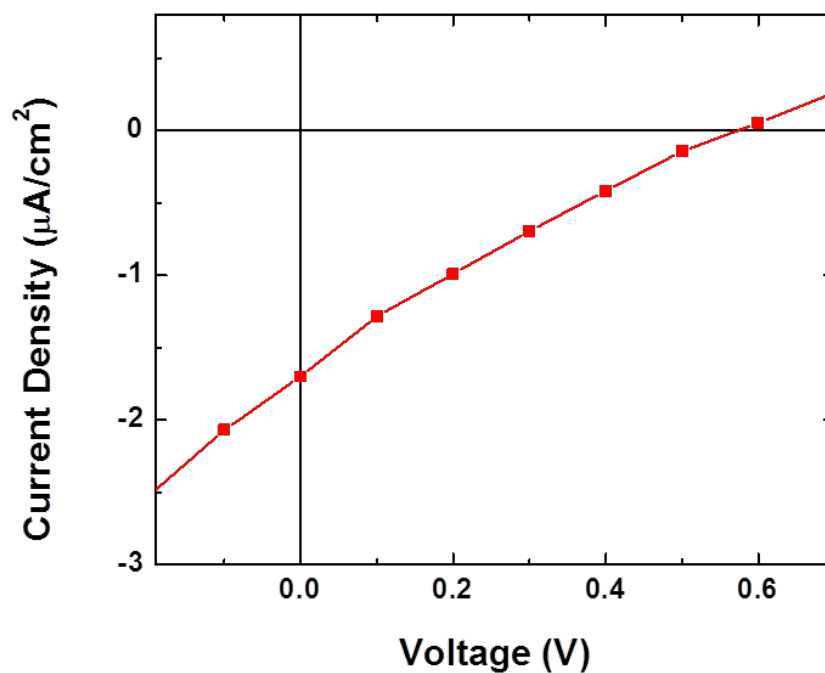


Figure 5.5. I-V characterization of the PSC devices (Au/Al/P3HT/PCBM/PEDOT:PSS/ITO) fabricated by the multi-layer inking and stamping.

5.4 Conclusion

In summary, a multi-layer pattern transfer from PDMS stamp to both ITO glass and PET flexible substrates in making polymer solar cells are demonstrated. SEM images show a clear

and clean pattern transfer, the transferred patterns were mostly free of deformities such as cracks or ripples. The cross-sectional SEM monograph indicates each layer is well defined after the pattern transfer. AFM image documents the recessions between transferred patterns, indicating good separation between PSC devices. It is found that incorporation of GLYMO into PEDOT:PSS is essential for successful pattern transfer and 5.0 μ l of GLYMO is the optimum amount needed per ml of PEDOT:PSS for both a high yield pattern transfer and a solar cell efficiency.

Although the multilayer inking and stamping technique for making polymer solar cells has been developed, much improvement of the device efficiency is still needed in order for this method to be comparable with those of solely spin-coated polymer solar cells and traditional inorganic solar cells. For example, possible future improvements could include finding a replacement for the GLYMO adhesive agent that better supports solar cell efficiency, and developing a procedure to produce more consistent separation between transferred patterns on a substrate while still maintaining an overall high yield pattern transfer. These improvements may ultimately help realize the multi-layer inking and stamping pattern transfer technique as a more viable and beneficial option for large-scale PSC fabrication.

CHAPTER 6

CONCLUSION AND FUTURE WORK

6.1 Conclusion

In this dissertation, I study the structure-property-performance relationship in organic thin-film transistors and polymer solar cells, and demonstrate one-step multilayer pattern transfer to make organic polymer solar cells on both glass and flexible substrates. To improve the charge transport and field-effect mobility in OTFTs, I applied combined CESA method and double solvent approach, and polymer additive as well to enhance crystal alignment and surface coverage, which are presented in Chapter 2. As for study on polymer solar cells, the effect of vertical composition profile on performance of organic solar cells is systematically investigated through computer simulation, and the physical principles behind the influence are deeply explained and analyzed (Chapter 3). In Chapter 4, ZnO electron transport layer in inverted organic solar cells structure was deposited by two different techniques, sol-gel method and ALD approach. The morphologies of ZnO film and nanorods have demonstrated significant influence on the efficiency of PSCs with inverted structure, which is one of the most important factors that affect the device. In Chapter 5, a pattern transfer technique, multilayer inking and stamping, was developed and demonstrated multilayer pattern transfer to make organic solar cells on both rigid

and flexible substrates, which could benefit organic polymer solar cell fabrication through roll-to-roll printing. The detailed description and conclusions on each study are as follows:

In Chapter 2, I first demonstrate the double solvent approach to increase the number of nucleation seeds and thus improving the coverage of crystals on the substrate. In this chapter, I also propose and use two different ways to well-align small molecule crystals: it controlled evaporative self-assembly (CESA) method and polymer additive. The greatly enhanced crystal alignment, film coverage and crystal width were observed with combined CESA method and double solvent approach. The effects of different ratios between the good solvent chloroform and bad solvent ethanol on crystal film morphology were investigated, and chloroform/ethanol at 5:1 volume ratio was found to lead to the optimal film morphology with the best crystal orientation, the highest film coverage and the largest crystal width. A mobility of $1.6 \times 10^{-2} \text{ cm}^2/\text{Vs}$ has been obtained. Polymer additive blended with small molecule was also demonstrated to be able to effectively align crystal growth. Both methods managed to get mobility much higher than ever reported in literature.

In Chapter 3, I systematically study the influence of active layer vertical configuration on performance of polymer solar cells. Five vertical configurations are modeled, Sandwich I, Sandwich II, Favorable, Unfavorable and Uniform. An investigation on the variation of open circuit voltage, short circuit current and fill factor was also carried out. Open circuit voltage depends on the accumulation of charge carriers at each end and absorbance. In the model, the absorbance for all five configurations is very similar, so the main difference comes from charge carrier accumulation. The more electrons at cathode and more holes at anode result in higher Voc. Short circuit current relies on external quantum efficiency, which is conversion rate from input photons to free charge carriers. Higher external quantum efficiency leads to higher short circuit

current. Fill factor mainly relies on the resistance, both series resistance and shunt resistance. It is ideal for a higher fill factor if the shunt resistance is infinitely great, while series resistance infinitely small. In both regular and inverted structures, Favorable and Uniform configurations always give the highest efficiency, while Sandwich and Unfavorable configurations tend to have poor performance. It is anticipated that such conclusions will be able to guide the development of the active layer in terms of vertical composition profile and push the efficiency of organic photovoltaic into a new level. In addition, the simulation study also provides an in-depth understanding of physical mechanisms behind the different vertical configurations of active layer and the effect on solar cell performance. .

Chapter 4 introduces two different methods, atomic layer deposition and sol-gel spin-coat, to fabricate both ZnO thin films and nanorods. The performance of organic solar cells using these ZnO layers as electron transport layer is compared. Devices based on ZnO films demonstrated higher efficiency than those from ZnO nanorods. Although nanorod morphology increases the interface between ZnO and active layer, the surface roughness, possible surface defects and increased charge transport resistance through nanorods cause overall series resistance increase, resulting in a poor performance and low efficiency. Compare ZnO films prepared by ALD deposition and sol-gel growth, solar cells with ZnO film made by sol-gel method show better performance (higher V_{oc} , I_{sc} and fill factor) thereby a higher efficiency due to lower surface roughness.

Chapter 5 demonstrates a multilayer pattern transfer technique to fabricate organic polymer solar cells on both ITO glass and flexible substrates. In this multilayer inking and stamping technique, flexible PDMS is used as a mold, and organic layers and metals are “inked” on the patterned PDMS mold. The protruded multi-layers are then transferred on pre-treated

substrate. From SEM and AFM images, transferred patterns are clean and clearly separated, and each layer is well defined. In the process of pattern transfer, adhesive agent, GLYMO, is a necessity additive in PEDOT:PSS solution since it increases the adhesion between PEDOT:PSS and substrate. However, too much GLYMO will decrease the efficiency of PSC devices. A balance of both well transfer pattern and good performance is found that 5.0 μ l of GLYMO is the optimum amount needed per ml of PEDOT:PSS for both a high yield pattern transfer and a solar cell efficiency. In addition, patterns are successfully transferred on flexible PET substrate with well separated patterns.

6.2 Future Work

From the study in this dissertation, new techniques and approaches have been developed and demonstrated the performance improvement on organic thin-film transistors and polymer solar cells. The research group has accumulated much experience on optimization of processing conditions and fabrication of OTFTs and OPVs. These methods could be applied to other material systems with better properties. For example, upon the success on crystal alignment and areal coverage from small molecule SMDPPEH, the combined CESA and dual solvent approach introduced in chapter 2 can be applied to performance organic small molecules, such as 2,7-dioctyl[1]benzothieno[3,2-b]benzothiophene (C8BTBT), which has been demonstrated the highest field-effect hole mobility, reaching up to 43 cm²/Vs. The conclusion on the effects of active layer vertical configuration on the performance of organic polymer solar cells could also be applied to guide experiments. Based on the simulation study, organic bulk heterojunction solar cells with uniform distribution of donor and acceptors have the best performance. One of

the potential way to alter vertical configuration is to add copolymer in the low-bandgap donor/acceptor blending system. By optimizing the amount of copolymer additive, a desirable uniform donor and acceptor distribution in the vertical direction could be obtained. By taking advantages of large spectrum absorption from low-bandgap polymers and favorable exciton dissociation and charge transport, the efficiency of the organic solar cells based on advanced materials systems could be further improved.

In this study the multilayer pattern transfer technique has been developed and successfully applied in making organic polymer solar cells. It is anticipated that this multilayer inking and stamping method could also work on fabrication of hybrid organic–inorganic perovskite solar cells, which have achieved the highest efficiency over 20%. Organometal halide perovskites are solution processible and present good optoelectric properties, such as long diffusion length, high carrier mobility, suitable optical bandgaps, and strong absorption of light. Such high efficiency and solution processing capability make perovskite solar cells a great potential for mass production through low-cost roll-to-roll printing on flexible substrates. For perovskite solar cells, two structures are commonly used, regular structure and inverted configuration, as shown in Figure 6(a) and Figure 6(b), respectively. In regular structure, ITO serves as anode with PEDOT:PSS as hole transport layer at the bottom, while low workfunction metal Al on the top acts as cathode with PCBM works as electron transport layer. In inverted structure, ITO at the bottom becomes cathode with TiO₂ as electron transport layer for electron collection, while high workfunction metal Au or Ag serves as anode at the top with spiro as the hole transport layer for hole collection.

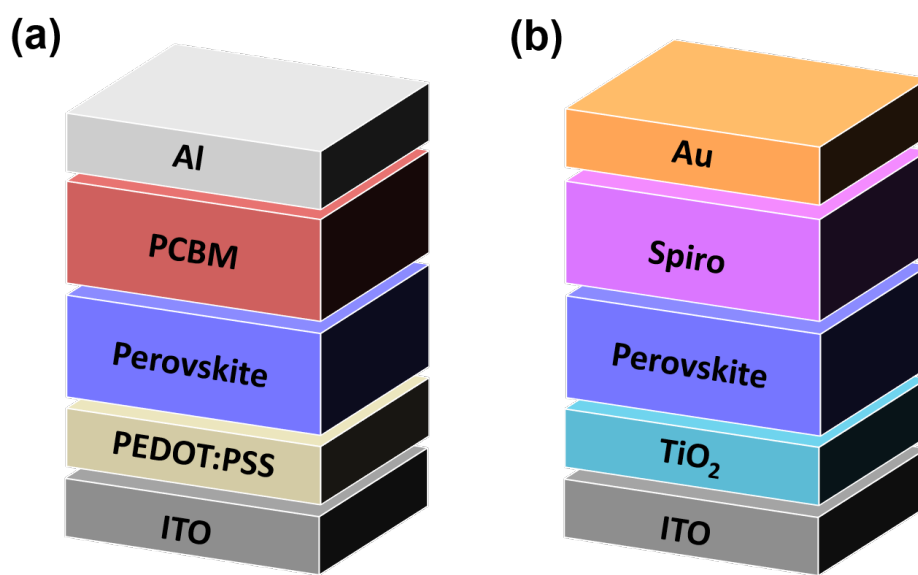


Figure 6. Schematic of perovskite solar cells with (a) regular and (b) inverted structures

Multilayer pattern transfer method could be applied in fabrication of both regular and inverted perovskite solar cells. In regular structure, a thin layer of gold could be sputtered on PDMS surface followed by first. Al deposition by thermal evaporation as demonstrated in Chapter 5. Then, PCBM electron transport layer, perovskite layer and PEDOT:PSS hole transport layer are spin-coated on top each other consequently. The inked PDMS mold will then be pressed onto pre-treated ITO glass for multilayer pattern transfer. In inverted structure, as top anode Au will be directly deposited on PDMS stamp because of low adhesion on it, followed by sequent deposition of hole transport layer, Spiro, perovskite active layer and TiO_2 as electron transport layer onto PDMS stamp with Au layer. The inked PDMS mold will be pressed onto pre-treated ITO glass to finalize the fabrication of perovskite solar cells with inverted structure. As indicated in Chapter 5, a proper amount of GLYMO will be necessary to increase the adhesion between PEDOT:PSS/ TiO_2 and ITO glass. The balance for improving pattern transfer yield

while maintain high efficiency has to be found in term of the concentration of GLYMO in PEDOT:PSS or TiO₂ solutions.

REFERENCES

1. A. J. Heeger, *Chemical Society Reviews* 39 (7), 2354-2371 (2010).
2. D. N. Congreve, J. Lee, N. J. Thompson, E. Hontz, S. R. Yost, P. D. Reuswig, M. E. Bahlke, S. Reineke, T. Van Voorhis and M. A. Baldo, *Science* 340 (6130), 334-337 (2013).
3. H. Cao, W. He, Y. Mao, X. Lin, K. Ishikawa, J. H. Dickerson and W. P. Hess, *Journal of Power Sources* 264, 168-183 (2014).
4. C. D. Dimitrakopoulos and P. R. L. Malenfant, *Advanced Materials* 14 (2), 99-+ (2002).
5. K. Nomura, H. Ohta, A. Takagi, T. Kamiya, M. Hirano and H. Hosono, *Nature* 432 (7016), 488-492 (2004).
6. S. Guenes, H. Neugebauer and N. S. Sariciftci, *Chemical Reviews* 107 (4), 1324-1338 (2007).
7. L. M. Kozycz, D. Gao, J. Hollinger and D. S. Seferos, *Macromolecules* 45 (14), 5823-5832 (2012).
8. N. Li, S. Oida, G. S. Tulevski, S.-J. Han, J. B. Hannon, D. K. Sadana and T.-C. Chen, *Nature Communications* 4 (2013).
9. M. S. AlSalhi, J. Alam, L. A. Dass and M. Raja, *International Journal of Molecular Sciences* 12 (3), 2036-2054 (2011).
10. C. Li, Y. Chen, Y. Zhao, H. Wang, W. Zhang, Y. Li, X. Yang, C. Ma, L. Chen, X. Zhu and Y. Tu, *Nanoscale* 5 (20), 9536-9540 (2013).

11. B. H. Wunsch, K. Kim, Y. Rho, B. Ahn, S. Jung, L. E. Polander, D. G. Bucknall, S. R. Marder and M. Ree, *Journal of Materials Chemistry C* 1 (4), 778-785 (2013).
12. Y. Lin, Y. Li and X. Zhan, *Chemical Society Reviews* 41 (11), 4245-4272 (2012).
13. H. Aziz, Z. D. Popovic, N. X. Hu, A. M. Hor and G. Xu, *Science* 283 (5409), 1900-1902 (1999).
14. M. Hedenqvist and U. W. Gedde, *Progress in Polymer Science* 21 (2), 299-333 (1996).
15. Y. Sun, J. Tao, G. G. Z. Zhang and L. Yu, *Journal of Pharmaceutical Sciences* 99 (9), 4023-4031 (2010).
16. S. K. Bhateja, S. M. Yarbrough and E. H. Andrews, *Journal of Macromolecular Science-Physics* B29 (1), 1-10 (1990).
17. E. Kun and K. Marossy, *Materials Science Forum* 752, 241-247 (2013).
18. P. Ravi, S. Dai, C. Wang and K. C. Tam, *Journal of Nanoscience and Nanotechnology* 7 (4-5), 1176-1196 (2007).
19. A. Kobayashi, K. Mine, T. Nakamura, M. Sasaki and K. Sawa, Patent No. EP869516-A1; JP10283843-A; KR98080834-A; US6074695-A; SG74621-A1; US6149966-A; TW419750-A; EP869516-B1; DE69807770-E; JP3415741-B2.
20. Y. Yuan, G. Giri, A. L. Ayzner, A. P. Zoombelt, S. C. B. Mannsfeld, J. Chen, D. Nordlund, M. F. Toney, J. Huang and Z. Bao, *Nature Communications* 5 (2014).
21. Z. He, J. Chen, Z. Sun, G. Szulczewski and D. Li, *Organic Electronics* 13 (10), 1819-1826 (2012).
22. X. Gao and Y. Hu, *Journal of Materials Chemistry C* 2 (17), 3099-3117 (2014).
23. J. H. Chen, M. Shao, K. Xiao, Z. R. He, D. W. Li, B. S. Lokitz, D. K. Hensley, S. M. Kilbey, J. E. Anthony, J. K. Keum, A. J. Rondinone, W. Y. Lee, S. Y. Hong and Z. A. Bao, *Chem. Mater.* 25 (21), 4378-4386 (2013).

24. C. W. Sele, B. K. C. Kjellander, B. Niesen, M. J. Thornton, J. van der Putten, K. Myny, H. J. Wondergem, A. Moser, R. Resel, A. van Breemen, N. van Aerle, P. Heremans, J. E. Anthony and G. H. Gelinck, *Adv. Mater.* 21 (48), 4926-+ (2009).
25. Z. R. He, S. Shaik, S. Bi, J. H. Chen and D. W. Li, *Appl. Phys. Lett.* 106 (18), 183301 (2015).
26. R. Hamilton, J. Smith, S. Ogier, M. Heeney, J. E. Anthony, I. McCulloch, J. Veres, D. D. C. Bradley and T. D. Anthopoulos, *Adv. Mater.* 21 (10-11), 1166-1171 (2009).
27. G. H. Gelinck, H. E. A. Huitema, E. Van Veenendaal, E. Cantatore, L. Schrijnemakers, J. Van der Putten, T. C. T. Geuns, M. Beenhakkers, J. B. Giesbers, B. H. Huisman, E. J. Meijer, E. M. Benito, F. J. Touwslager, A. W. Marsman, B. J. E. Van Rens and D. M. De Leeuw, *Nature Mater.* 3 (2), 106-110 (2004).
28. D. W. Li, E. J. Borkent, R. Nortrup, H. Moon, H. Katz and Z. N. Bao, *Appl. Phys. Lett.* 86 (4), 042105 (2005).
29. I. Bae, S. J. Kang, Y. J. Shin, Y. J. Park, R. H. Kim, F. Mathevet and C. Park, *Adv. Mater.* 23 (30), 3398-+ (2011).
30. Z. R. He, K. Xiao, W. Durant, D. K. Hensley, J. E. Anthony, K. L. Hong, S. M. Kilbey, J. H. Chen and D. W. Li, *Adv. Func. Mater.* 21 (19), 3617-3623 (2011).
31. Z. R. He, D. W. Li, D. K. Hensley, A. J. Rondinone and J. H. Chen, *Appl. Phys. Lett.* 103 (11), 113301 (2013).
32. K. Asare-Yeboah, R. M. Frazier, G. Szulczewski and D. W. Li, *J. Vac. Sci. Tech. B* 32 (5), 052401 (2014).
33. D. T. James, J. M. Frost, J. Wade, J. Nelson and J. S. Kim, *Acs Nano* 7 (9), 7983-7991 (2013).
34. Z. R. He, N. Lopez, X. L. Chi and D. W. Li, *Org. Electron.* 22, 191-196 (2015).

35. W. H. Lee, D. H. Kim, Y. Jang, J. H. Cho, M. Hwang, Y. D. Park, Y. H. Kim, J. I. Han and K. Cho, *Appl. Phys. Lett.* 90 (13), 132106 (2007).
36. H. Y. Li, B. C. K. Tee, J. J. Cha, Y. Cui, J. W. Chung, S. Y. Lee and Z. N. Bao, *J. Am. Chem. Soc.* 134 (5), 2760-2765 (2012).
37. W. Han, M. Byun, L. Zhao, J. Rzayev and Z. Lin, *J. Mater. Chem.* 21 (37), 14248-14253 (2011).
38. S. W. Kwon, M. Byun, D. H. Yoon, J.-H. Park, W.-K. Kim, Z. Lin and W. S. Yang, *J. Mater. Chem.* 21 (14), 5230-5233 (2011).
39. W. Han and Z. Q. Lin, *Angew. Chem. Int. Ed.* 51 (7), 1534-1546 (2012).
40. D. H. Kim, D. Y. Lee, H. S. Lee, W. H. Lee, Y. H. Kim, J. I. Han and K. Cho, *Adv. Mater.* 19 (5), 678-+ (2007).
41. H. Minemawari, T. Yamada and T. Hasegawa, *Japan. J. Appl. Phys.* 53 (5) (2014).
42. G. Q. Zhang, K. Liu, Y. Li and M. J. Yang, *Polymer International* 58 (6), 665-673 (2009).
43. M. Akita, I. Osaka and K. Takimiya, *Materials* 6 (3), 1061-1071 (2013).
44. M. J. Cho, J. Shin, S. H. Yoon, T. W. Lee, M. Kaur and D. H. Choi, *Chemical Communications* 49 (64), 7132-7134 (2013).
45. L. T. Dou, J. Gao, E. Richard, J. B. You, C. C. Chen, K. C. Cha, Y. J. He, G. Li and Y. Yang, *Journal of the American Chemical Society* 134 (24), 10071-10079 (2012).
46. J. Ajuria, S. Chavhan, R. Tena-Zaera, J. H. Chen, A. J. Rondinone, P. Sonar, A. Dodabalapur and R. Pacios, *Organic Electronics* 14 (1), 326-334 (2013).
47. J. W. Lee, Y. S. Choi and W. H. Jo, *Organic Electronics* 13 (12), 3060-3066 (2012).
48. S. Y. Qu and H. Tian, *Chem. Comm.* 48 (25), 3039-3051 (2012).

49. A. B. Tamayo, X.-D. Dang, B. Walker, J. Seo, T. Kent and T.-Q. Nguyen, *Appl. Phys. Lett.* 94 (10) (2009).
50. K. Sakamoto, J. Ueno, K. Bulgarevich and K. Miki, *Appl. Phys. Lett.* 100 (12) (2012).
51. Y. Li, S. P. Singh and P. Sonar, *Adv. Mater.* 22 (43), 4862-+ (2010).
52. A. D. Hendsbee, J.-P. Sun, L. R. Rutledge, I. G. Hill and G. C. Welch, *Journal of Materials Chemistry A* 2 (12), 4198-4207 (2014).
53. C. Kanimozhi, N. Yaacobi-Gross, E. K. Burnett, A. L. Briseno, T. D. Anthopoulos, U. Salzner and S. Patil, *Phys. Chem. Chem. Phys.* 16 (32), 17253-17265 (2014).
54. J. S. Zambounis, Z. Hao and A. Iqbal, *Nature* 388 (6638), 131-132 (1997).
55. Z. R. He, J. H. Chen, J. K. Keum, G. Szulczewski and D. W. Li, *Org. Electron.* 15 (1), 150-155 (2014).
56. Z. R. He, J. H. Chen, Z. Z. Sun, G. Szulczewski and D. W. Li, *Org. Electron.* 13 (10), 1819-1826 (2012).
57. R. D. Deegan, O. Bakajin, T. F. Dupont, G. Huber, S. R. Nagel and T. A. Witten, *Nature* 389 (6653), 827-829 (1997).
58. R. D. Deegan, O. Bakajin, T. F. Dupont, G. Huber, S. R. Nagel and T. A. Witten, *Physical Review E* 62 (1), 756-765 (2000).
59. X. R. Li, B. K. C. Kjellander, J. E. Anthony, C. W. M. Bastiaansen, D. J. Broer and G. H. Gelinck, *Adv. Func. Mater.* 19 (22), 3610-3617 (2009).
60. J. Zhou, Y. Zuo, X. Wan, G. Long, Q. Zhang, W. Ni, Y. Liu, Z. Li, G. He, C. Li, B. Kan, M. Li and Y. Chen, *Journal of the American Chemical Society* 135 (23), 8484-8487 (2013).
61. J. You, C.-C. Chen, Z. Hong, K. Yoshimura, K. Ohya, R. Xu, S. Ye, J. Gao, G. Li and Y. Yang, *Advanced Materials* 25 (29), 3973-3978 (2013).

62. P. Kumar and S. Chand, *Progress in Photovoltaics* 20 (4), 377-415 (2012).
63. M. O. Reese, M. S. White, G. Rumbles, D. S. Ginley and S. E. Shaheen, *Applied Physics Letters* 92 (5) (2008).
64. Y. Sun, G. C. Welch, W. L. Leong, C. J. Takacs, G. C. Bazan and A. J. Heeger, *Nature Materials* 11 (1), 44-48 (2012).
65. B. Walker, A. B. Tomayo, X.-D. Dang, P. Zalar, J. H. Seo, A. Garcia, M. Tantiwiwat and T.-Q. Nguyen, *Advanced Functional Materials* 19 (19), 3063-3069 (2009).
66. J. You, L. Dou, K. Yoshimura, T. Kato, K. Ohya, T. Moriarty, K. Emery, C.-C. Chen, J. Gao, G. Li and Y. Yang, *Nature Communications* 4 (2013).
67. M. Campoy-Quiles, T. Ferenczi, T. Agostinelli, P. G. Etchegoin, Y. Kim, T. D. Anthopoulos, P. N. Stavrinou, D. D. C. Bradley and J. Nelson, *Nature Materials* 7 (2), 158-164 (2008).
68. B. Xue, B. Vaughan, C.-H. Poh, K. B. Burke, L. Thomsen, A. Stapleton, X. Zhou, G. W. Bryant, W. Belcher and P. C. Dastoor, *Journal of Physical Chemistry C* 114 (37), 15797-15805 (2010).
69. H.-X. Wei, Y.-Q. Li, X.-Y. Chen, C.-S. Lee and J.-X. Tang, *Organic Electronics* 15 (11), 2810-2816 (2014).
70. E. Danielson, Z.-E. Ooi, K. Liang, J. Morris, C. Lombardo and A. Dodabalapur, *Journal of Photonics for Energy* 4 (2014).
71. Z. Xu, L.-M. Chen, G. Yang, C.-H. Huang, J. Hou, Y. Wu, G. Li, C.-S. Hsu and Y. Yang, *Advanced Functional Materials* 19 (8), 1227-1234 (2009).
72. S. S. van Bavel, E. Sourty, G. de With and J. Loos, *Nano Letters* 9 (2), 507-513 (2009).

73. Z. Z. Sun, K. Xiao, J. K. Keum, X. Yu, K. L. Hong, J. Browning, I. N. Ivanov, J. H. Chen, J. Alonzo, D. W. Li, B. G. Sumpter, E. A. Payzant, C. M. Rouleau and D. B. Geohegan, *Advanced Materials* 23 (46), 5529-+ (2011).
74. M. T. Neukom, N. A. Reinke and B. Ruhstaller, *Solar Energy* 85 (6), 1250-1256 (2011).
75. M. T. Neukom, S. Zuefle and B. Ruhstaller, *Organic Electronics* 13 (12), 2910-2916 (2012).
76. M. Shibao, T. Morita, W. Takashima and K. Kaneto, *Japanese Journal of Applied Physics Part 2-Letters & Express Letters* 46 (4-7), L123-L125 (2007).
77. J. Nakamura, K. Murata and K. Takahashi, *Applied Physics Letters* 87 (13) (2005).
78. E. von Hauff, V. Dyakonov and R. Parisi, *Solar Energy Materials and Solar Cells* 87 (1-4), 149-156 (2005).
79. C. Tanase, E. J. Meijer, P. W. M. Blom and D. M. de Leeuw, *Physical Review Letters* 91 (21) (2003).
80. A. Pivrikas, N. S. Sariciftci, G. Juska and R. Osterbacka, *Progress in Photovoltaics* 15 (8), 677-696 (2007).
81. A. Pivrikas, H. Neugebauer and N. S. Sariciftci, *Ieee Journal of Selected Topics in Quantum Electronics* 16 (6), 1746-1758 (2010).
82. Y.-T. Tsai, K. Goto, O. Yoshikawa, S. Mori, T. Sagawa and S. Yoshikawa, *Japanese Journal of Applied Physics* 50 (1) (2011).
83. F. Hamdani, A. Botchkarev, W. Kim, H. Morkoc, M. Yeadon, J. M. Gibson, S. C. Y. Tsen, D. J. Smith, K. Evans, C. W. Litton, W. C. Mitchel and P. Hemenger, *Applied Physics Letters* 70 (4), 467-469 (1997).
84. K. Nomura, H. Ohta, K. Ueda, T. Kamiya, M. Hirano and H. Hosono, *Science* 300 (5623), 1269-1272 (2003).

85. Y.-H. Chou, B.-T. Chou, C.-K. Chiang, Y.-Y. Lai, C.-T. Yang, H. Li, T.-R. Lin, C.-C. Lin, H.-C. Kuo, S.-C. Wang and T.-C. Lu, *Acs Nano* 9 (4), 3978-3983 (2015).
86. C. T. Lee, Y. K. Su and H. M. Wang, *Thin Solid Films* 150 (2-3), 283-289 (1987).
87. H. Y. Dang, J. Wang and S. S. Fan, *Nanotechnology* 14 (7), 738-741 (2003).
88. H. Zhang, D. Yang, X. Y. Ma, Y. J. Ji, J. Xu and D. L. Que, *Nanotechnology* 15 (5), 622-626 (2004).
89. K. Keis, E. Magnusson, H. Lindstrom, S. E. Lindquist and A. Hagfeldt, *Solar Energy Materials and Solar Cells* 73 (1), 51-58 (2002).
90. V. C. Sousa, A. M. Segadaes, M. R. Morelli and R. Kiminami, *International Journal of Inorganic Materials* 1 (3-4), 235-241 (1999).
91. A. Qurashi, N. Tabet, M. Faiz and T. Yamzaki, *Nanoscale Research Letters* 4 (8), 948-954 (2009).
92. X. J. Zheng, X. C. Cao, J. Sun, B. Yuan, Q. H. Li, Z. Zhu and Y. Zhang, *Nanotechnology* 22 (43) (2011).
93. S. K. Hau, H.-L. Yip, N. S. Baek, J. Zou, K. O'Malley and A. K. Y. Jen, *Applied Physics Letters* 92 (25) (2008).
94. A. K. K. Kyaw, X. W. Sun, C. Y. Jiang, G. Q. Lo, D. W. Zhao and D. L. Kwong, *Applied Physics Letters* 93 (22) (2008).
95. S. K. Hau, H.-L. Yip, H. Ma and A. K. Y. Jen, *Applied Physics Letters* 93 (23) (2008).
96. D. Wohrle and D. Meissner, *Advanced Materials* 3 (3), 129-138 (1991).
97. Y. Zhang, T. P. Basel, B. R. Gautam, X. M. Yang, D. J. Mascaró, F. Liu and Z. V. Vardeny, *Nature Communications* 3 (2012).

98. J. U. Lee, J. W. Jung, T. Emrick, T. P. Russell and W. H. Jo, *Nanotechnology* 21 (10) (2010).
99. M.-G. Kang, M.-S. Kim, J. Kim and L. J. Guo, *Advanced Materials* 20 (23), 4408-4413 (2008).
100. K.-S. Chen, H.-L. Yip, J.-F. Salinas, Y.-X. Xu, C.-C. Chueh and A. K. Y. Jen, *Advanced Materials* 26 (20), 3349-+ (2014).
101. F. C. Krebs, S. A. Gevorgyan and J. Alstrup, *Journal of Materials Chemistry* 19 (30), 5442-5451 (2009).
102. J. Park, K. Shin and C. Lee, *Robotics and Computer-Integrated Manufacturing* 30 (5), 432-441 (2014).
103. M. Helgesen, J. E. Carle, J. Helt-Hansen, A. Miller and F. C. Krebs, *Journal of Applied Polymer Science* 131 (18) (2014).
104. D. Kaduwal, H.-F. Schleiermacher, J. Schulz-Gericke, T. Kroyer, B. Zimmermann and U. Wuerfel, *Solar Energy Materials and Solar Cells* 124, 92-97 (2014).
105. T. R. Andersen, H. F. Dam, M. Hosel, M. Helgesen, J. E. Carle, T. T. Larsen-Olsen, S. A. Gevorgyan, J. W. Andreasen, J. Adams, N. Li, F. Machui, G. D. Spyropoulos, T. Ameri, N. Lemaitre, M. Legros, A. Scheel, D. Gaiser, K. Kreul, S. Berny, O. R. Lozman, S. Nordman, M. Valimaki, M. Vilkmann, R. R. Sondergaard, M. Jorgensen, C. J. Brabec and F. C. Krebs, *Energy & Environmental Science* 7 (9), 2925-2933 (2014).
106. K.-H. Choi, J.-A. Jeong, J.-W. Kang, D.-G. Kim, J. K. Kim, S.-I. Na, D.-Y. Kim, S.-S. Kim and H.-K. Kim, *Solar Energy Materials and Solar Cells* 93 (8), 1248-1255 (2009).
107. F. C. Krebs, V. Senkovskyy and A. Kiriya, *Ieee Journal of Selected Topics in Quantum Electronics* 16 (6), 1821-1826 (2010).
108. D. Li and L. J. Guo, *Journal of Physics D-Applied Physics* 41 (10) (2008).
109. D. W. Li and L. J. Guo, *Applied Physics Letters* 88 (6) (2006).

110. M. A. Meitl, Z. T. Zhu, V. Kumar, K. J. Lee, X. Feng, Y. Y. Huang, I. Adesida, R. G. Nuzzo and J. A. Rogers, *Nature Materials* 5 (1), 33-38 (2006).
111. N. Bowden, S. Brittain, A. G. Evans, J. W. Hutchinson and G. M. Whitesides, *Nature* 393 (6681), 146-149 (1998).
112. M. Kang, H. Kim, B. W. Han, J. Suh, J. Park and M. Choi, *Microelectronic Engineering* 71 (2), 229-236 (2004).
113. J.-W. Kim, K.-Y. Yang, S.-H. Hong and H. Lee, *Applied Surface Science* 254 (17), 5607-5611 (2008).
114. H. Schmid, H. Wolf, R. Allenspach, H. Riel, S. Karg, B. Michel and E. Delamarche, *Advanced Functional Materials* 13 (2), 145-153 (2003).
115. E. Menard, L. Bilhaut, J. Zaumseil and J. A. Rogers, *Langmuir* 20 (16), 6871-6878 (2004).

APPENDIX

LIST OF PUBLICATIONS AND PRESENTATIONS

Journal Publications

1. **Sheng Bi**, Che-Nan Sun, Thomas A. Zawodzinski Jr., FeiRen, Jong KahkKeum, Suk-KyunAhn, Dawen Li,* Jihua Chen*, “Reciprocated Suppression of Polymer Crystallization towards Improved Solid Polymer Electrolytes: Tunable Ion Conductivity and Mechanical Properties”, *Journal of Polymer Science: Polymer Physics*, 53, (2015)
2. **Sheng Bi**, Zhengran He, Jihua Chen, and Dawen Li*, “Solution-Grown Small-Molecule Organic Semiconductor with Enhanced Crystal Alignment and Areal Coverage for Organic Thin Film Transistors”, *AIP Advances*, Vol. 5, Issue 7 (2015)
3. KyeiwaaAsare – Yeboah, **Sheng Bi**, Zhengran He, and Dawen Li*, “Temperature Gradient Controlled Crystal Growth from TIPS Pentacene-Poly(α -methyl styrene) Blends for Improving Performance of Organic Thin Film Transistors”, *Organic Electronics*, 32, (2016)
4. Zhengran He, Shoieb Shaik, **Sheng Bi** and Dawen Li*, “Air-Stable Solution-Processed n-Channel Organic Thin Film Transistors with Polymer-Enhanced Morphology”, *Applied Physics Letter*, 106, (2015)
5. Che-Nan Sun, Thomas A. Zawodzinski Jr., Wyatt E. Tenhaeff, FeiRen, Jong KahkKeum, **Sheng Bi**, Dawen Li, Suk-KyunAhn, Kunlun Hong, Adam J. Rondinone, Jan-Michael Y. Carrillo, Changwoo Do, Bobby G. Sumpter, Jihua Chen*, “Nanoscale Enhanced Ionic Transport in Fullerene Reinforced Solid Polymer Electrolytes”, *Physical Chemistry Chemical Physics*, 2015, 17, 8266-8275

Conference Presentations

1. **Sheng Bi**, Zhongliang Ouyang, Dawen Li*, “Solution-Grown Small-Molecule Organic Semiconductor with Enhanced Crystal Alignment and Areal Coverage for Organic Thin Film Transistors”, Center for Materials for Information Technology Review and Workshop, (2015)
2. **Sheng Bi**, Dawen Li*, “Organic Polymer Solar Cells Patterned By Multi-Layer Inking and Stamping”, Center for Materials for Information Technology Review and Workshop, (2014)
3. **Sheng Bi**, Zhenzhong Sun, Dawen Li*, “Improvement of P3HT/PCBM Photovoltaic Efficiency through Vertical Composition Optimization”, Materials Research Society, San Francisco, (2014)
4. **Sheng Bi**, Zhengran He, Dawen Li*, “DPP Single Crystal Growth and Alignment for Improving Charge Transport”, Science and Technology Open House sponsored by NSF Alabama EPSCOR, Montgomery, AL, (2014)
5. **Sheng Bi**, Zhenzhong Sun, Dawen Li*, “Improvement of P3HT/PCBM Photovoltaic Efficiency through Vertical Composition Optimization”, Center for Materials for Information Technology Review and Workshop, (2013)
6. **Sheng Bi**, Zhengran He, Dawen Li*, “Vertical Configuration Effect for P3HT-PCBM Based Active Layer”, Science and Technology Open House sponsored by NSF Alabama EPSCOR, Montgomery, AL, (2013)